AGU PUBLICATIONS

JGR

Journal of Geophysical Research: Space Physics

RESEARCH ARTICLE
10.1002/2014JA020454

Key Points:
- Vertical emissivity profiles of Jovian IR aurora were resolved in K band
- H_3^+ overtone and hot overtone lines had lower peak altitudes than the model
- This lower peak was caused by the non-LTE effect stronger than the model

Correspondence to:
Y. Kasaba,
kasaba@pat.gp.tohoku.ac.jp

Citation:
Uno, T., Y. Kasaba, C. Tao, T. Sakanoi, M. Kagitani, S. Fujisawa, H. Kita, and S. V. Badman (2014), Vertical emissivity profiles of Jupiter's northern H_3^+ and H_2 infrared auroras observed by Subaru/IRCS, *J. Geophys. Res. Space Physics*, *119*, 10,219–10,241, doi:10.1002/2014JA020454.

Received 31 JUL 2014
Accepted 5 NOV 2014
Accepted article online 7 NOV 2014
Published online 3 DEC 2014

Vertical emissivity profiles of Jupiter's northern H_3^+ and H_2 infrared auroras observed by Subaru/IRCS

T. Uno[1], Y. Kasaba[1], C. Tao[2], T. Sakanoi[3], M. Kagitani[3], S. Fujisawa[1], H. Kita[3], and S. V. Badman[4]

[1]Department of Geophysics, Tohoku University, Sendai, Japan, [2]Institut de Recherche en Astrophysique et Planétologie, Université de Toulouse, CNRS, Toulouse, France, [3]Planetary Plasma and Atmospheric Research Center, Tohoku University, Sendai, Japan, [4]Department of Physics, Lancaster University, Lancaster, UK

Abstract We resolved the vertical emissivity profiles of H_3^+ overtone, H_3^+ hot overtone, and H_2 emission lines of the Jovian northern auroras in K band obtained in December 2011 observed by the IR Camera and Spectrograph of the Subaru 8.2 m telescope with the adaptive optics system (AO188). The spatial resolution achieved was ~0.2 arcsec, corresponding to ~600 km at Jupiter. We derived the vertical emissivity profiles at three polar regions close to the Jovian limb. The H_3^+ overtone and H_3^+ hot overtone lines had similar peak altitudes of 700–900 km and 680–950 km above the 1 bar level, which were 100–300 km and 150–420 km lower, respectively, than the model values. On the contrary, the H_2 peak emission altitude was high, 590–720 km above the 1 bar level. It was consistent with the value expected for precipitation of ~1 keV electron, which favors a higher-altitude emissivity profile. We concluded that the lower peak altitudes of H_3^+ overtone and hot overtone lines were caused by the nonlocal thermodynamic equilibrium effect stronger than the model assumption. We could reproduce the observational emissivity profiles from the model by including this effect. It has been proposed that neutral H_2 and ionized H_3^+ emissions can have different source altitudes because of their different morphologies and velocities; however, our observed results with a general circulation model show that the peak emission altitudes of H_3^+ and H_2 can be similar even with different velocities.

1. Introduction

Jupiter has a highly dynamic magnetosphere. Its dominant energy is derived from its fast planetary rotation. It is transported from the neutral atmosphere to the magnetosphere through ion-neutral interactions in the polar thermosphere and ionosphere and drives the Jovian magnetosphere, ionosphere, and thermosphere (MIT) coupling system. As the feedback from this system, the polar upper atmosphere is subject to precipitating particles, ion drag, and Joule heating. The activity of this region can be remotely observed via intense Jovian aurora at ultraviolet (UV) and infrared (IR) wavelengths [e.g., *Badman et al.*, 2014, and references therein]. The IR aurora results from H_3^+ fundamental transitions ($v_2 = 1$–0) in the L band around 3–4 μm, H_3^+ overtone ($v_2 = 2$–0), H_3^+ hot overtone ($v_2 = 3$–1), and H_2 S_1 ($v = 1$–0) transitions in the K band around 2–2.5 μm [e.g., *Drossart et al.*, 1989; *Miller et al.*, 1990; *Kim et al.*, 1990]. In the K band, ionized (H_3^+) and neutral (H_2) hydrogen lines can be observed simultaneously from ground-based telescopes.

The vertical emissivity profiles of this region have been studied in both UV and IR auroras. A self-consistent one-dimensional (1-D) model of the vertical atmospheric and emissivity profiles in the Jovian polar upper atmosphere was proposed by *Grodent et al.* [2001] for discrete and diffuse aurora cases. This model predicted the peak emission altitude at ~250 km above the 1 bar pressure level for UV H_2 aurora and at ~400–500 km for IR H_3^+ fundamental transitions under the local thermodynamic equilibrium (LTE) condition. Based on this model, *Cohen and Clarke* [2011] simulated the altitudinal emission profiles of Jupiter's UV auroral emission and evaluated its scale height above the limb position by comparison with the images taken by the Hubble Space Telescope (HST). The observed scale height in the northern hemisphere (~400–600 km in their Figure 4) agreed with the model emissivity scale height (~250–300 km) within a factor of 1–2, whereas that in the southern hemisphere (~500–800 km in their Figure 5) was higher, which suggests a higher temperature in the south than that in the north.

The vertical volume emissivity profile of the IR H_3^+ aurora should be affected by thermal collisions because the population of excited vibrational levels departs from LTE at higher altitudes. This non-LTE effect [e.g., *Kim et al.*, 1992] predicts that above the altitude of ~650 km, the population of vibrational excited

levels would be lower than that under LTE conditions since the radiative deexcitation (time scale: A_{if} in Table 2) would occur on a time scale faster than the collisional excitation in the lower-density environment found at higher altitudes. By this effect, the populations in higher states with faster A_{if} are lower than those in the LTE case. This effect should appear in observations as a lower peak altitude and scale height of H_3^+ overtone ($v_2 = 2$–0) and hot overtone ($v_2 = 3$–1) emissions from higher states. *Melin et al.* [2005] simulated their altitudinal profiles to include this effect. The estimated peak emission altitude became ~1000 km for the H_3^+ overtone transitions and ~1100 km for the H_3^+ hot overtone transitions in the non-LTE case. These altitudes were higher than that of the H_3^+ fundamental line, ~550 km (in both non-LTE and LTE cases), because overtone and hot overtone lines were more enhanced in higher thermospheric temperatures at higher altitudes. However, they were lower than the values expected under LTE conditions, ~1500–1600 km. The scale heights of the H_3^+ overtone and hot overtone transitions were also slightly reduced from ~600 km in the LTE case to ~500 km in the non-LTE case.

For IR H_2 emissions, although the vertical emission profile was not derived theoretically, its peak altitude can be considered as that of the number density of H_2 in the $v = 1$ state, which is affected by the energy of precipitating electrons. The estimated peak altitude was located at ~700, ~450, and ~280 km for precipitating electrons with energies of 1, 10, and 100 keV, respectively [*Cravens*, 1987; *Kim*, 1988].

For the observations of H_3^+ fundamental lines observed in the L band, *Lystrup et al.* [2008] evaluated the vertical profile using slit spectroscopy with the near-infrared spectrograph on the Keck II telescope. Although the spatial resolution in the observation was 0.74 arcsec (~1000 km on Jupiter), the vertical profiles with higher resolution were derived by the "onion peeling method" with the emissivity profile modeled as a series of concentric shells. Identification of the peak altitude was not attempted because it was difficult to resolve the location of the limb position accurately. However, their results showed that the scale height of the H_3^+ ion density (~350–400 km) in the region above the peak emission altitude up to ~1800 km was similar to that in the model of *Grodent et al.* [2001] when modified with the non-LTE effect. (We note that this observation was made in the southern hemisphere. As previously mentioned in *Cohen and Clarke* [2011], the southern UV H_2 aurora had a larger scale height than that in the northern hemisphere and in the Grodent model.)

In the K band containing H_3^+ overtone lines, H_3^+ hot overtone lines, and H_2 lines, no similar trials have been reported thus far. An indirect suggestion was made by *Raynaud et al.* [2004] from the temperature profile derived from observations using the Fourier transform spectrometer (FTS/BEAR) on the Canada–France–Hawaii Telescope. In their results, H_3^+ overtone lines showed a higher rotational temperature, ~1170 K, which is similar to the temperature from the hot band H_3^+ in the L band, 900–1250 K [*Stallard et al.*, 2002]. According to the expected altitudinal temperature profile in *Grodent et al.* [2001], which has a strong positive temperature gradient of typically 200 K per decade in pressure, the researchers suggested that H_3^+ overtone and H_3^+ hot overtone lines were emitted from a higher (hotter) region at ~1400 km altitude. For the observations of infrared H_2 lines such as H_3^+, *Kim et al.* [1990] discussed the vertical profile based on the observed H_2 temperature, ~730 (+490 to −200) K. From this lower temperature, they estimated the H_2 peak emission altitude as ~500–700 km, which is lower than those of H_3^+ overtone and hot overtone lines.

Another clue to the altitude of H_3^+ and H_2 emissions comes from the difference in their auroral horizontal morphologies: *Raynaud et al.* [2004] showed that H_2 and H_3^+ emissions in the K band have different latitude-longitude distributions. This suggests a difference in their emission altitudes, heating process, and the energy transfer between the ionized and neutral polar atmospheres. From the same data set, *Chaufray et al.* [2011] showed that the line of sight velocity of H_2 molecules, determined from the Doppler shift of the emission lines, was <1.0 km/s, which is lower than that of the H_3^+ ions measured at 3.1 ± 0.4 km/s. This result could have originated from the difference in altitudes sounded by these emission lines. Similar differences in the H_2 and H_3^+ morphology and velocity field have also been confirmed by Infrared Telescope Facility echelle spectroscopy in the K band [*Uno*, 2013].

In this paper, we derive the vertical emissivity profiles of K band H_3^+ and H_2 auroral emissions in the Jovian northern hemisphere with high spatial resolution data assisted by adaptive optics. Data were taken in December 2011 using the IR Camera and Spectrograph (IRCS) attached to the Subaru 8.2 m telescope. The observations simultaneously covered a wide wavelength range of 1.95–2.41 μm, including multiple H_3^+

Table 1. Summary of the Observed Data Set Used in This Study on 1 December 2011

	Time (UT)	Central Meridian Longitude (System-III)	Air Mass
AO1	9:34–39	259°	1.14
AO2	9:44–49	265°	1.17
AO3	9:50–55	269°	1.18

overtone lines, H_3^+ hot overtone lines, and H_2 lines in the same field of view along the slit. Such simultaneity is essential for the better comparison of H_3^+ and H_2 lines whose horizontal distributions should be different. This observation was supported by the adaptive optics system AO188 locked onto Europa (diameter: ~1 arcsec), and achieved a spatial resolution of ~0.2 arcsec, corresponding to ~600 km at Jupiter. Three data sets crossing the northern polar limb region enabled us to compare the vertical emissivity profiles between the ionized (H_3^+) and neutral (H_2) components with reasonable accuracy and spatial resolution.

2. Observation and Analysis

2.1. Observation and Data Reduction

The observations were performed on 1 December 2011. The Jovian equatorial angular diameter was 47.5 arcsec (~3010 km/arcsec), and the subobserver latitude was 3.6°. We used an echelle spectrometer IRCS (InfraRed Camera and Spectrograph) [*Kobayashi et al.*, 2000] attached to the Subaru 8.2 m telescope at Mauna Kea, Hawaii. The IRCS is a cross-dispersed echelle spectrometer covering a wavelength range of 1–5 μm. It has a 1024 × 1024 InSb array detector with a pixel resolution of 0.055 (along slit: 165 km at Jupiter) × 0.068 (vertical to slit: 204 km at Jupiter) arcsec^2. IRCS has an infrared camera used as the slit viewer. Its detector is a 1024 × 1024 InSb array with a pixel resolution of 0.053 × 0.053 arcsec^2 (160 × 160 km^2 at Jupiter). In this paper, we analyzed the three data sets listed in Table 1 when the 188-element Adaptive Optics module (AO188) [*Hayano et al.*, 2008, 2010; *Minowa et al.*, 2010] was activated.

Figure 1 shows an example of an observed spectrum (AO2 in Table 1). The IRCS echelle and cross disperser gratings were set to cover the wavelength range of 1.95–2.41 μm, which was distributed over six diffraction orders (24–29). Although several gaps with the width of ~0.02–0.04 μm occur between neighboring orders,

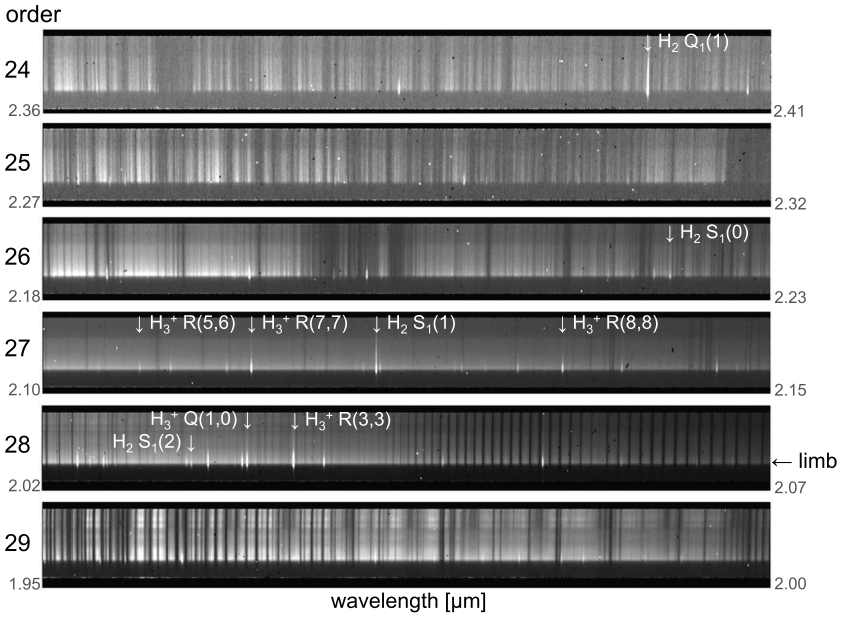

Figure 1. An example spectral image observed by Subaru/IRCS during AO2 (9:44–9:49, 1 December 2011). The six landscape bands are the echelle order of 29 (1.954–1.999 μm), 28 (2.024–2.071 μm), 27 (2.099–2.148 μm), 26 (2.179–2.230 μm), 25 (2.266–2.319 μm), and 24 (2.361–2.416 μm). Several H_3^+ and H_2 emission lines are marked. The background continuum above the position of the limb is scattering light from the Jovian disk.

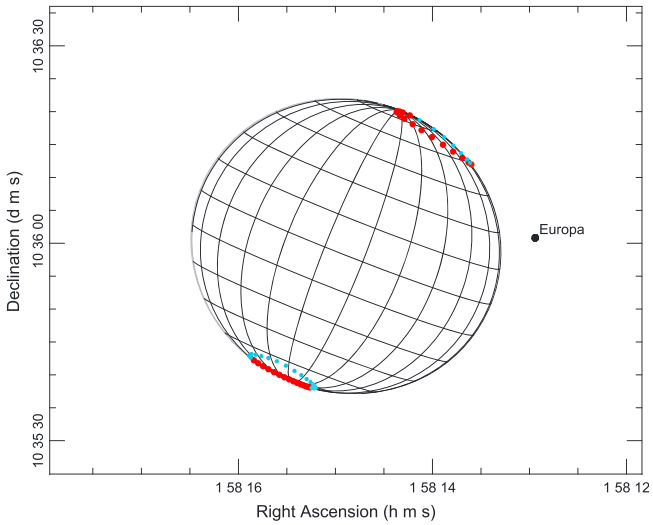

Figure 2. The geometry of Jupiter and Europa at 09:45 UT on 1 December 2011 modified from the output of Rings Node On-line Tools (http://pds-rings.seti.org/tools/). Circles indicate the expected main auroral location in front of the limb (red) and beyond (blue) in the statistics of UV aurora [*Nichols et al.*, 2009].

this setup enabled us to observe multiple H_3^+ and H_2 emission lines simultaneously at the same slit location. We used a slit size of 0.14×5.17 arcsec^2 ($427 \times 15{,}560$ km^2 at Jupiter) from which the spectral resolution $\lambda/d\lambda$ was 18,300–22,300. The slit was set along the Jovian rotation axis that was almost perpendicular to the limb. In Figure 1, the lower part of each panel is the region of space above the limb. The continuum component from the Jovian disk is visible over the entire wavelength range. Overlapping terrestrial absorption lines were used for wavelength calibration. The spatial error over the entire spectral range was less than 0.2 pixel (~30 km), which represents the accuracy of the relative spatial distributions between H_3^+ overtone, H_3^+ hot overtone, and H_2 emission profiles.

We identified the Jovian limb position at the pixel of the limb-brightening peak in this Jovian disk continuum component. Since it is at same position along the wide spectral range, its position accuracy was ~1 pixel (~165 km). The identification of this altitude affects the absolute altitude of the vertical emission profile. This limb-brightening peak is caused by scattered light from the stratospheric polar haze and is seen at latitudes greater than +60°. The number density of the polar haze derived by Cassini imaging observation has a maximum at the ~10–20 mbar level at a latitude of +75°, ~90 km above the 1 bar level [*Zhang et al.*, 2013]. *Mallama et al.* [2000] used the Callisto eclipse light curve and reported that the upper limit of detectable photometric absorption by the polar haze may be up to ~300 km above the 1 bar level at a latitude of +88°. Although we thought that 90–100 km seemed more feasible, we assumed in this paper that the observed limb-brightening position is between these values, at an altitude of 200 ± 100 km above the 1 bar level. In the following analysis, this altitude is used as the base in the absolute altitude determination.

We obtained three spectral data sets (AO1, AO2, and AO3 in Table 1), while the AO188 system was activated during 09:30–10:00 UT. Without AO, the seeing was ~0.8 arcsec (full width at half maximum (FWHM)). During the activation of AO188 using Europa as a guide star, the effective seeing was improved to ~0.2 arcsec (FWHM), corresponding to ~600 km at Jupiter. Europa's distance from Jupiter's northern pole was ~50–25 arcsec (Figure 2).

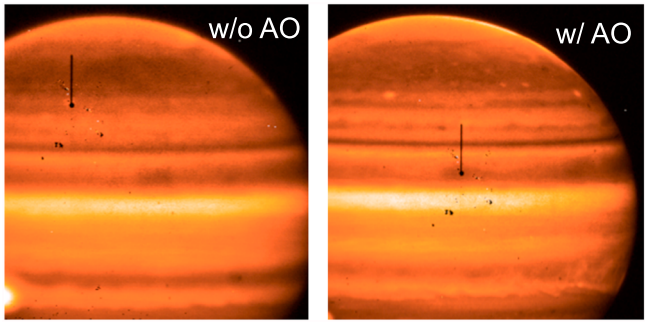

Figure 3. Jovian images taken by the IRCS slit viewer with wideband K-band filter. (left)An image without AO188 (seeing: ~0.8 arcsec, 5:10 UT on 1 December 2011). (right) An image with AO188 (seeing: ~0.2 arcsec, 8:28 UT on 1 December 2011). The black vertical lines parallel to Jupiter's rotation axis on the Jovian disk are the slit images (length: 5.17 arcsec; width: 0.14 arcsec).

Although this resolution is lower than that of the of UV aurora studies with HST [e.g., *Cohen and Clarke*, 2011], it enabled us to extract the vertical profile, i.e., emission peak altitude and scale height, with the resolution close to 1 pixel (~165 km) by the onion peeling method as described in section 2.2. Observations were made in AB node patterns in which A was the object and B was the sky. Each spectrum with an integration time of 300 s achieved over more than counts for strong H_3^+ and H_2 emission lines with signal-to-noise (S/N) ratios of

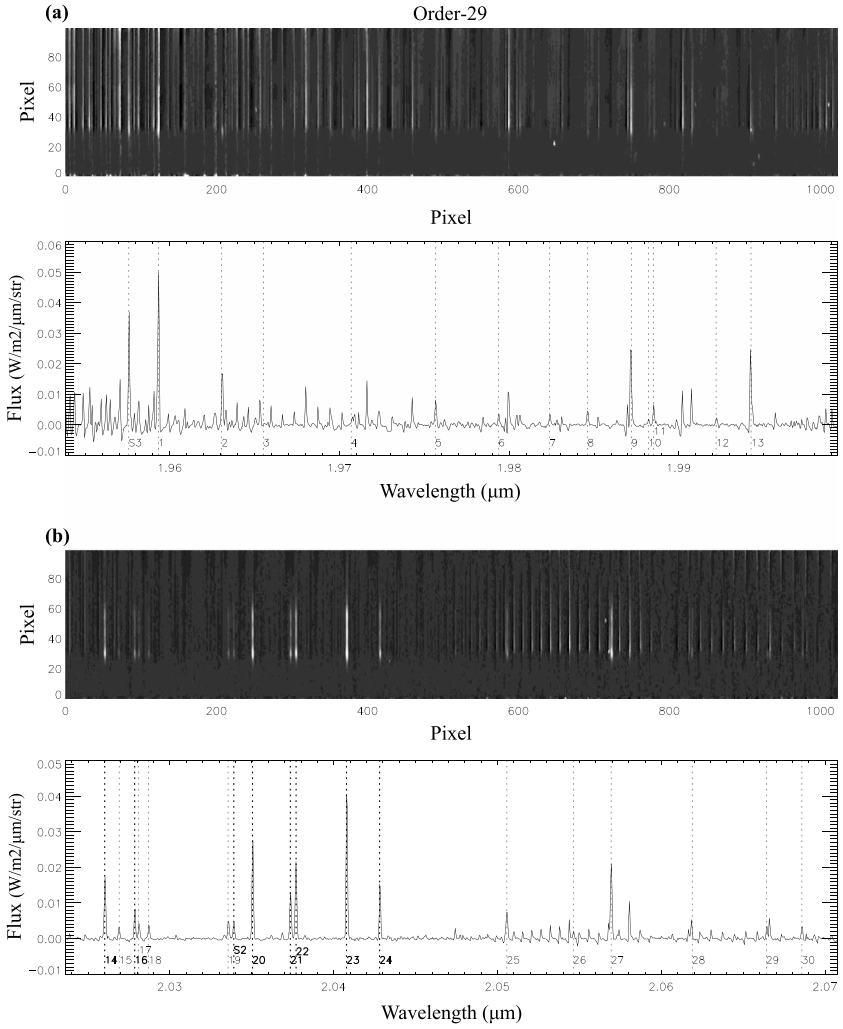

Figure 4. The spectrum of AO1. The wavelength ranges are (a) 1.954–1.999 μm (order 29), (b) 2.024–2.071 μm (order 28), (c) 2.099–2.148 μm (order 27), (d) 2.179–2.230 μm (order 26), (e) 2.266–2.319 μm (order 25), and (f) 2.361–2.416 μm (order 24). In each set of spectra, the (top row) shows the reduced spectral image (limb: at pixel #33; disk: upward), and the (bottom row) shows the cross-sectional cut of the spectral image at pixel #30, the brightest position above the limb. The flux is given in W/m^2/μm/str. The dotted vertical lines mark the detected H_3^+ (Table 2) and H_2 (Table 3) lines.

~60. We also obtained slit viewer images with the K-band wideband filter (Figure 3). It contained no auroral profiles but was used for identification of the slit position relative to the expected main aurora position shown in Figure 2. For wavelength and flux calibrations, the spectra of standard stars were taken at the beginning (HD 15318) and end (HD 15318 and HD 33777) of the observation using the same slit width as AO188, in which the effective seeing was ~0.1 arcsec. This value is better than that achieved for Jupiter because the AO guide star, Europa, was not a point source with a diameter of ~1 arcsec. In the flux calibration, we considered the flux outside the slit, ~40%, using the difference of on-slit and off-slit fluxes in the slit viewer data.

Data reduction was based on IRCS standard guidelines [*Pyo*, 2003]. We subtracted the mean of two sky frames (~1000 counts) before and after each object frame. An offset bias was also subtracted in each quadrant with different values (<100 counts) derived from nonilluminated regions. Flat fielding, bad pixel correction, cosmic ray correction, and aperture extraction were also applied. Finally, we subtracted a Jovian disk continuum component using a boxcar median [e.g., *Raynaud et al.*, 2004]. The box width was chosen as ~1.8×10^{-3} μm (~40 pixels), which is more than 20 times the width of a typical line, ~8×10^{-5} μm (~2 pixels) and was broadened by instrumental functions.

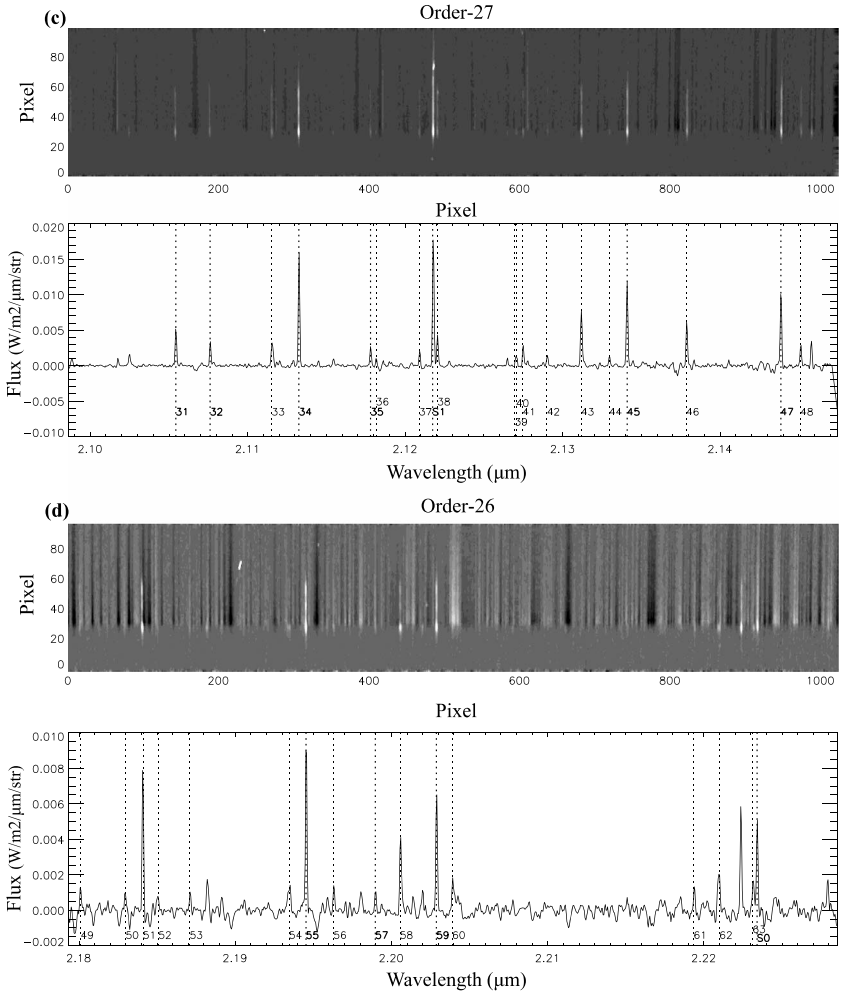

Figure 4. (continued)

Figure 4 shows the observed spectra of AO1 at the wavelength of 1.954–1.999 μm (order 29) (Figure 4a), 2.024–2.071 μm (order 28) (Figure 4b), 2.099–2.148 μm (order 27) (Figure 4c), 2.179–2.230 μm (order 26) (Figure 4d), 2.266–2.319 μm (order 25) (Figure 4e), and 2.361–2.416 μm (order 24) (Figure 4f). The limb-brightening peak position is at pixel #33. For each order, the top and bottom rows show the reduced spectral image and its cross section at pixel #30 at the brightest area of the emission lines, which is ~500 km above the limb-brightening peak.

Tables 2 and 3 summarize the 77 H_3^+ lines and 6 H_2 lines detected in Figure 4 using the lists of spectral lines in *Lindsay and McCall* [2001], *Neale et al.* [1996], *Kao et al.* [1991], *Dabrowski* [1984], and *Turner et al.* [1977]. This is the first time that several of H_3^+ overtone and hot overtone lines have been reported in the observations of Jupiter (*italic font* in Table 2). The index numbers in Tables 2 and 3 are indicated in Figure 4 at the wavelength of these H_3^+ or H_2 emissions marked with dotted vertical lines. For the following analysis, we selected the emission lines that satisfied the following conditions: (1) lower terrestrial absorption, with a terrestrial atmosphere transmittance larger than 0.8; (2) bright flux with a peak intensity of >0.001 W/m^2/μm/str, corresponding to S/N~10; (3) auroral profile on the Jovian disk that can be identified even on the disk continuum; and (4) other emission or absorption lines not overlapped within ±3 pixels. For the H_3^+ lines in Table 2, we used 15 overtone lines ($\nu_2 = 2$–0), marked by asterisk: 14, 16, 20, 21, 22, 23, 24, 32, 34, 45, 47, 55, 59, 70, and 77; and 5 hot overtone lines ($\nu_2 = 3$–1), marked by double asterisk: 31, 35, 57, 65, and 73. For the H_2 lines in Table 3, we used 3 S_1 lines at 2.22, 2.12, and 2.03 μm, marked by triple asterisk.

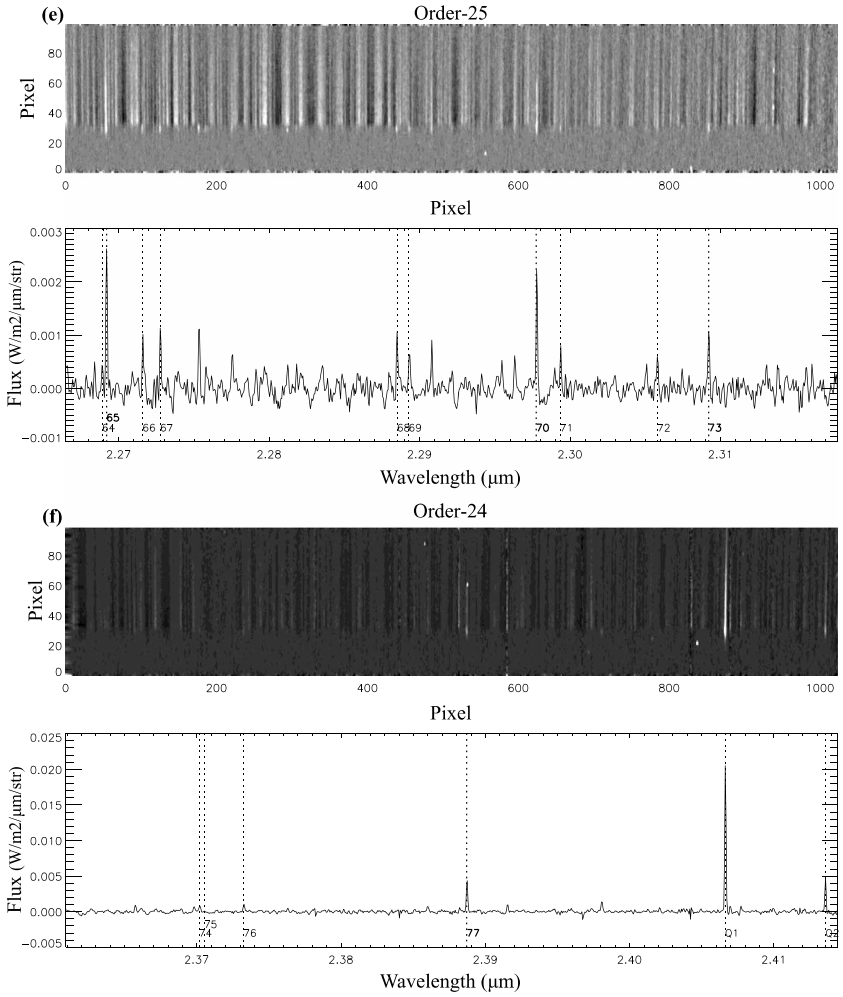

Figure 4. (continued)

2.2. Extraction of Vertical Emission Profiles

The observed spectra above the limb-brightening position, assumed as ~200(±100) km above 1 bar level in this paper (section 2.1), were integrated along the line of sight and contained the emission just above, in front of, and behind the limb at different altitudes. In order to extract the altitudinal distribution from each spectral image, we adopted the onion peeling method [e.g., *Lystrup et al.*, 2008] in which atmospheric emission layers are vertically divided into multiple horizontal shells with uniform emissivity. We set the thickness of each shell as equal to the pixel scale (0.055 arcsec, 165 km at Jupiter). The *N*th shell has an altitude of 165 (*N*-1)–165 *N* km from the Jovian limb (*N* = 1: just above the limb). We set the maximum *N* as 25, 19, and 19 for the AO1, AO2, and AO3 data, respectively, from the limitation of the field in the spectral image. These limits correspond to altitudes of ~4100 km for AO1 and ~3150 km for AO2 and AO3 from the limb.

We estimated the error of this method using the simulated flux distributions along the slit with the observed seeing of ~0.2 arcsec [*Uno*, 2013]. The emulated distribution was created from the 11 vertical emissivity profile models for the 5 H_2 cases (in 1 keV and 10 keV electron precipitation [*Cravens*, 1987], in 100 keV electron precipitation [*Kim*, 1988], and in UV and IR [*Grodent et al.*, 2001]) and six H_3^+ cases (fundamental, overtone, and hot overtone in LTE and non-LTE [*Melin et al.*, 2005]), respectively. All were horizontally uniform. From these emulated slit image data, we derived the vertical volume emissivity profile by the onion peeling method as applied to the actual observed data. Although these 11 vertical emissivity profile models had different peak altitudes and scale heights, the extracted profiles

Table 2. Spectroscopic Properties of the Detected H_3^+ Emission Lines in Figure 4[a]

No.	Order	λ (μm)	Flux (W/m^2/μm/str)	Assign.	ν_2	A_{if} (/s)	J′	g	E′ (/cm)	E″ (/cm)
1	*29*	*1.9592*	*0.051*	*R(5,3)*	*2–0*	*81.3*	*6*	*4*	*6120.4*	*1016.4*
2	*29*	*1.9630*	*0.017*	*^{t}R(1,0)*	*2–0*	*90.0*	*2*	*4*	*5117.1*	*22.8*
3	*29*	*1.9649*	*<0.001*	*P*		*98.2*	*7*	*2*	*6672.4*	*1583.1*
4	*29*	*1.9707*	*0.003*	*R*		*88.0*	*7*	*2*	*6441.0*	*1366.6*
5	*29*	*1.9756*	*0.008*	*^{t}R(2,1)*	*2–0*	*69.1*	*3*	*2*	*5235.1*	*173.2*
6	*29*	*1.9793*	*0.003*	*P*		*50.7*	*6*	*4*	*6574.8*	*1522.5*
7	*29*	*1.9823*	*0.003*	*R*		*93.2*	*8*	*8/3*	*6798.7*	*1754.0*
8	*29*	*1.9845*	*0.003*	*Q(3.1)*	*2–0*	*64.1*	*3*	*2*	*5469.6*	*430.6*
9	*29*	*1.9871*	*0.025*	*^{t}R(3,2)*	*2–0*	*87.0*	*4*	*2*	*5396.3*	*363.9*
10	*29*	*1.9881*	*0.001*	*P*		*80.4*	*7*	*2*	*6938.5*	*1908.7*
11	*29*	*1.9884*	*0.006*	*^{n}Q(2,1)*	*2–0*	*69.9*	*2*	*2*	*5202.3*	*173.2*
12	*29*	*1.9921*	*0.002*	*Q*	*3–1*	*75.5*	*7*	*4*	*7276.0*	*2256.3*
13	*29*	*1.9941*	*0.025*	*R*	*3–1*	*96.6*	*9*	*4*	*7192.8*	*2178.1*
14 *	**28**	**2.0259**	**0.017**	***^{t}R(2,2)***	**2–0**	**111.9**	**3**	**2**	**5041.2**	**105.2**
15	*28*	*2.0268*	*0.003*	*P*		*149.5*	*0*	*2*	*4933.9*	*0.0*
16 *	**28**	**2.0277**	**0.008**	***^{t}R(6,5)***	**2–0**	**115.8**	**7**	**2**	**6105.9**	**1174.3**
17	28	2.0280	0.004	^{n}P(6,5)^l	2–0	78.9	5	2	6105.3	1174.3
18	*28*	*2.0286*	*0.004*	*P*		*42.3*	*6*	*4*	*6452.0*	*1522.5*
19	*28*	*2.0334*	*0.005*	*P(5,4)*	*2–0*	*93.8*	*4*	*2*	*5782.7*	*864.8*
20 *	**28**	**2.0349**	**0.027**	***^{t}Q(3,0)***	**2–0**	**145.8**	**3**	**4**	**5367.0**	**452.8**
21 *	***28***	***2.0372***	***0.013***	***^{n}P(4,3)***	***2-0***	***98.4***	***3***	***4***	***5503.3***	***594.6***
22 *	**28**	**2.0375**	**0.022**	***^{t}Q(1,0)***	**2–0**	**152.5**	**1**	**4**	**4930.7**	**22.8**
23 *	**28**	**2.0407**	**0.041**	***^{t}R(3,3)***	**2–0**	**124.7**	**4**	**4**	**5151.6**	**251.2**
24 *	**28**	**2.0427**	**0.015**	***^{t}R(7,6)***	**2–0**	**121.3**	**8**	**4**	**6418.0**	**1522.5**
25	28	2.0505	0.008	^{n}P(3,2)	2–0	96.4	2	2	5240.8	363.9
26	*28*	*2.0546*	*0.002*	*Q*		*70.8*	*6*	*2*	*6544.0*	*1676.8*
27	28	2.0569	0.021	^{t}R(4,4)	2–0	134.1	5	2	5299.7	437.9
28	*28*	*2.0617*	*0.005*	*^{n}P(2,1)*	*2–0*	75.3	1	2	5023.5	173.2
29	*28*	*2.0663*	*0.005*	*^{t}Q(5,1)*	*2–0*	*73.4*	*5*	*2*	*6025.7*	*1186.2*
30	*28*	*2.0684*	*0.003*	*P*		*16.1*	*5*	*4*	*5766.3*	*931.7*
31 **	**27**	**2.1053**	**0.005**	***R(5,6)***	**3–1**	**346.7**	**6**	**4**	**7733.2**	**2983.3**
32 *	**27**	**2.1076**	**0.003**	***^{n}P(5,2)^u***	**2–0**	**62.0**	**4**	**2**	**5867.8**	**1123.0**
33	27	2.1115	0.003	^{t}Q(6,2)	2–0	71.4	6	2	6351.6	1615.7
34 *	**27**	**2.1131**	**0.016**	***^{t}R(7,7)***	**2–0**	**155.4**	**8**	**2**	**5970.5**	**1238.0**
35 **	**27**	**2.1176**	**0.002**	***R(6,7)***	**3–1**	**364.1**	**7**	**8/3**	**7927.8**	**3205.5**
36	*27*	*2.1180*	*0.001*	*^{n}P(4,3)$_l$*	*3–1*	*154.0*	*3*	*4*	*7802.7*	*3081.2*
37	27	2.1210	0.003	P(7,6)	2–0	20.9	6	4	6237.3	1522.5
38	27	2.1221	0.004	^{t}Q(5,2)	2–0	67.0	5	2	5835.3	1123.0
39	27	2.1271	*0.001*	P(6,5)	2–0	13.3	5	2	5875.6	1174.3
40	27	2.1272	*0.001*	P(8,7)	2–0	24.3	7	2	6609.7	1908.7
41	27	2.1276	0.003	^{n}P(4,1)	2–0	56.4	3	2	5469.6	769.5
42	*27*	*2.1291*	*0.002*	*P*		*45.5*	*5*	*2*	*6312.4*	*1615.7*
43	*27*	*2.1313*	*0.008*	*^{t}Q(4,2)*	*2–0*	*58.9*	*4*	*2*	*5396.3*	*704.4*
44	*27*	*2.1331*	*0.001*	*Q*	*3–1*	*54.3*	*8*	*4*	*7399.6*	*2711.5*
45 *	**27**	**2.1337**	**0.012**	***^{t}R(8,8)***	**2–0**	**161.8**	**9**	**8/3**	**6269.9**	**1583.1**
46	27	2.1380	0.006	^{t}Q(3,2)	2–0	42.1	3	2	5041.2	363.9
47 *	**27**	**2.1439**	**0.011**	***^{t}P(3,0)***	**2–0**	**63.8**	**2**	**4**	**5117.1**	**452.8**
48	*27*	*2.1452*	*0.003*	*^{n}P(7,3)*	*2–0*	*69.3*	*6*	*4*	*6739.6*	*2078.0*
49	26	2.1800	0.001	P(6,1)	2–0	45.0	5	2	6263.8	1676.8
50	*26*	*2.1829*	*0.001*	*R*	*3–1*	*58.2*	*3*	*4*	*7329.9*	*2748.7*
51	*26*	*2.1840*	*0.008*	*^{t}Q(5,3)*	*2–0*	*51.2*	*5*	*4*	*5595.1*	*1016.4*
52	*26*	*2.1850*	*0.001*	*P*		*14.5*	*6*	*2*	*6330.7*	*1754.0*
53	*26*	*2.1870*	*0.001*	*P*		*10.9*	*5*	*2*	*5939.0*	*1366.6*
54	*26*	*2.1934*	*0.001*	*Q*		*9.3*	*5*	*4*	*5766.3*	*1207.1*
55*	**26**	**2.1944**	**0.009**	***^{t}Q(4,3)***	**2–0**	**34.6**	**4**	**4**	**5151.6**	**594.6**
56	*26*	*2.1962*	*0.001*	*^{t}Q(4,3)$_u$*	*3–1*	131.2	4	4	7722.7	3169.3
57*	***26***	***2.1989***	***0.001***	***Q***	***3–1***	**53.6**	**8**	**8/3**	**7122.8**	**2575.0**
58	*26*	*2.2005*	*0.004*	*R*	*3–1*	*115.5*	*6*	*4*	*8033.6*	*3489.2*
59 *	***26***	***2.2028***	***0.006***	***^{t}P(5,0)***	***2–0***	***70.6***	***4***	***4***	***5746.9***	***1207.1***
60	*26*	*2.2038*	*0.002*	*R(3.1)*	*2–0*	*10.2*	*2*	*2*	*4968.3*	*430.6*
61	*26*	*2.2193*	*0.001*	*R*	*3–1*	*103.2*	*2*	*4*	*7058.5*	*2552.6*

Table 2. (continued)

No.	Order	λ (μm)	Flux (W/m^2/μm/str)	Assign.	v_2	A_{if} (/s)	J′	g	E′ (/cm)	E″ (/cm)
62	*26*	*2.2209*	*0.002*	*Q*		*52.2*	*7*	*2*	*6441.0*	*1938.3*
63	*26*	*2.2231*	*0.002*	*P*	*3–1*	*112.6*	*3*	*2*	*7298.1*	*2799.8*
64	*25*	*2.2689*	*<0.001*	*P*	*3–1*	*100.9*	*3*	*4*	*7790.4*	*3382.9*
65***	***25***	***2.2692***	***0.003***	***R***	***3–1***	***148.8***	***5***	***4***	***7488.0***	***3081.2***
66	*25*	*2.2716*	*0.001*	*Q*		*18.9*	*4*	*2*	*5588.4*	*1186.2*
67	*25*	*2.2728*	*0.001*	*Q*		*47.3*	*8*	*8/3*	*6798.7*	*2398.7*
68	*25*	*2.2885*	*0.001*	*P*	*3–1*	*165.7*	*6*	*2*	*7702.2*	*3332.4*
69	*25*	*2.2894*	*<0.001*	*Q*	*3–1*	*97.2*	*3*	*4*	*7329.9*	*2961.8*
70*	***25***	***2.2978***	***0.002***	***Q(7,5)***	***2–0***	***40.9***	***7***	***2***	***6105.9***	***1754.0***
71	*25*	*2.2994*	*<0.001*	*P(6,1)*	*2–0*	*19.8*	*5*	*2*	*6025.7*	*1676.8*
72	*25*	*2.3058*	*<0.001*	*P(4,2)*	*2–0*	*5.8*	*3*	*2*	*5041.2*	*704.4*
73 **	***25***	***2.3091***	***0.001***	***R***	***3–1***	***181.3***	***7***	***2***	***7951.7***	***3621.0***
74	*24*	*2.3699*	*<0.001*	*P*		*12.4*	*5*	*2*	*5835.3*	*1615.7*
75	*24*	*2.3702*	*<0.001*	*P*		*15.4*	*6*	*2*	*6397.0*	*2177.9*
76	*24*	*2.3730*	*<0.001*	*P*		*26.2*	*7*	*4*	*6925.7*	*2711.5*
77*	***24***	***2.3885***	***0.004***	***Q(7,6)***	***2–0***	***24.2***	***7***	***4***	***5709.1***	***1522.5***

[a]The "v_2" column is (2–0): overtone ($v_2 = 2 \rightarrow 0$) and (3–1): hot overtone ($v_2 = 3 \rightarrow 1$), respectively. The "Flux' column is the peak flux in AO1 at pixel #31 (Figure 4). The bold font indicates the data used in section 3 (single asterisk: 15 overtone lines (14, 16, 20, 21, 22, 23, 24, 32, 34, 45, 47, 55, 59, 70, and 77; $v_2 = 2 \rightarrow 0$) and double asterisk: 5 hot overtone lines (31, 35, 57, 65, and 73; $v_2 = 3 \rightarrow 1$)). The italic font indicates the first time detected line at Jupiter. References are *Neale et al.* [1996] with *Lindsay and McCall* [2001] and *Kao et al.* [1991].

were similar to the original: The peak altitudes had good agreement with an error of 100–200 km from the model values, and the emission scale height also agreed when the original scale height was more than ~100 km.

This method assumes (1) an optically thin emission source and (2) horizontally uniform emissivity in each shell. The former is applicable in the region of focus in this study. For the latter, we know that the Jovian aurora is not uniform. If a narrower but brighter main oval component is not at the limb but in front of or behind it, it can enhance the flux closer to the limb in the slit image and potentially create a lower peak altitude in the emissivity profile derived by the onion peeling method. When the emission source is in front of or behind the limb at the latitudinal and longitudinal angular difference θ, the emission source at height h_0 is seen at the distance from the limb h:

$$h = (R_0 + h_0)\cos\theta - R_0 \tag{1}$$

where R_0 is the Jovian radius, ~70,000 km. The observed flux at the position h contains the integrated emission across the shell (165 km thickness) at the height of h_0 along the line of sight length L:

$$L \sim 2\left(\sqrt{\left(R_0 + h_0 + \frac{165[\mathrm{km}]}{2}\right)^2 - (R_0 + h)^2} - \sqrt{\left(R_0 + h_0 - \frac{165[\mathrm{km}]}{2}\right)^2 - (R_0 + h)^2}\right). \tag{2}$$

For example, the emission source at the height of $h_0 = 1000$ km can be seen at the distance from the limb of $h = 1000$, 830, 660, 500, 330, 170, and 0 km when $\theta = 0°$, 4°, 6°, 7°, 8°, 9°, and 10° with the line of sight

Table 3. Spectroscopic Properties of the Detected H_2 Emission Lines in Figure 4[a]

No.	Order	λ (μm)	Flux (W/m^2/str/μm)	Assign.	v_2	A_{if} (/s)	g	E′ × 10^{-7}
S_3	29	1.9576	0.038	S(3)	1–0	4.21	33	8365.0
S_2***	**28**	**2.0338**	**0.004**	**S(2)**	**1–0**	**3.98**	**9**	**7584.0**
S_1***	**27**	**2.1218**	**0.018**	**S(1)**	**1–0**	**3.47**	**21**	**6956.0**
S_0 ***	**26**	**2.2235**	**0.005**	**S(0)**	**1–0**	**2.53**	**5**	**6471.0**
Q_1	24	2.4066	0.021	Q(1)	1–0	4.29	9	6149.0
Q_2	24	2.4134	0.005	Q(2)	1–0	3.03	5	6471.0

[a]The flux column is the peak flux in AO1 at pixel #31 (Figure 4). The bold font indicates the data used in section 3, three lines (S_2, S_1, and S_0 with ***: S_1 ($v = 1 \rightarrow 0$)). Reference is *Dabrowski* [1984] with *Turner et al.* [1977].

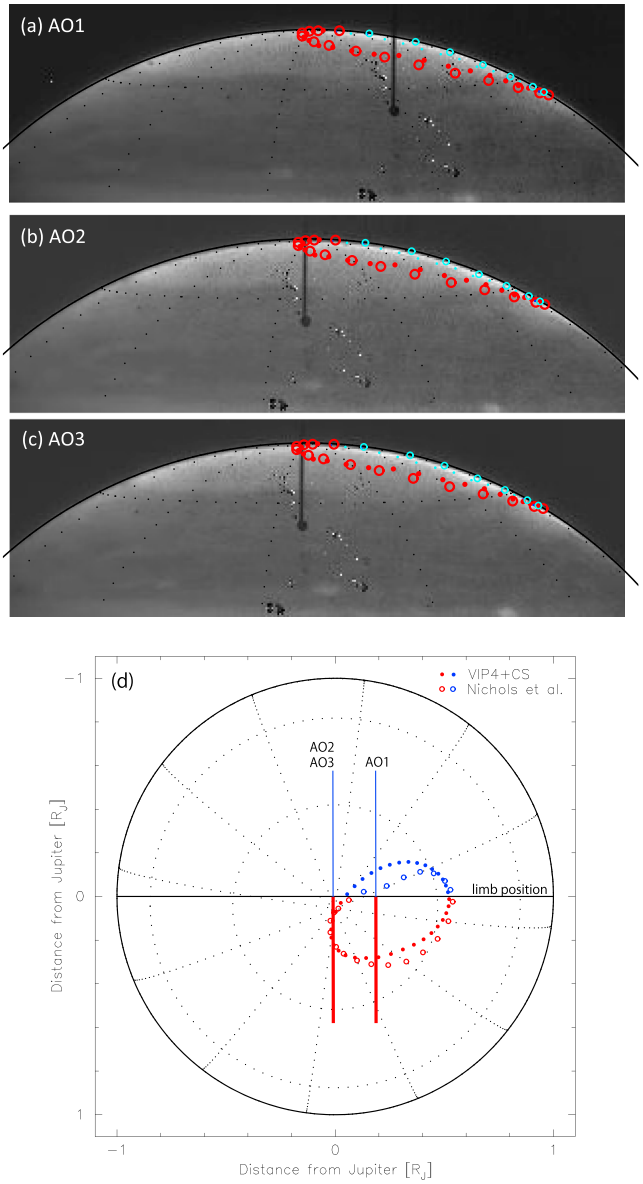

Figure 5. Slit viewer image of the Jovian northern polar region with K-band filter, (a) AO1, (b) AO2, and (c) AO3. The black vertical lines are the slit images (width: 0.14 arcsec; length: 5.17 arcsec) set parallel to Jupiter's rotation axis. Circles indicate the expected main auroral location in front of the limb (red) and behind it (blue). Large circles are the statistical location from UV aurora [*Nichols et al.*, 2009]. Smaller ones are from VIP4 + current sheet model [*Connerney et al.*, 1998; *Khurana*, 1997]. (d) Expected main oval position in northern polar view. Slit positions in AO1 and AO2/AO3 are also indicated. The red is the part in front of the limb. The blue is the part above the limb.

length of $L = 7000$, 5000, 3400, 2800, 2400, 2200, and 2000 km, respectively. This result means that (1) the averaged flux from wide range around the limb (~7000 km, $\theta = -3°$~+3°) can contribute to the flux at h~h_0, and (2) the bright flux from the area in front of and behind the limb ($\theta = -3$~−10 and +3°~+10°) contributes to the flux at $h < h_0$ but with a shorter line of sight length. This means that a weaker but wider auroral component around the limb position is more dominant in the observed slit image above the limb than a stronger but narrower component.

Figure 5 shows the K-band image of the slit position in AO1 (Figure 5a), AO2 (Figure 5b), and AO3 (Figure 5c), with the expected auroral main oval position (Figure 5d). In Figures 5a–5c, the black vertical lines on the Jovian disk are the slit images (0.14 × 5.17 arcsec). For the reference, the circles show the expected location of the northern main oval in two cases. Large circles indicate the statistical location from UV aurora observed during the Hubble Space Telescope 2007 campaign [*Nichols et al.*, 2009]. The smaller circles indicate the one expected at the foot print of 30 R_J in the VIP4 field model [*Connerney et al.*, 1998] modified with the current sheet model [*Khurana*, 1997]. In both models, we showed the positions not only in front of the limb (red) but also behind it (blue).

Although the estimated positions of the main oval depend on models and should not completely be the same with the one during our observations, we could check the possible flux contained in each slit position from Figure 5. In AO1, the slit position is across the main oval in front of the limb expected at 1.1–1.3 arcsec (20–24 pixels, 3300–4000 km) inside, far from the limb. We also find that the main oval behind the limb might be close, at 0.04–0.19 arcsec (0.7–3.5 pixels, 110–580 km) inside. Therefore, the flux above the limb appears to be dominated by polar diffuse aurora but may also contain the main oval just behind the horizon which can show the virtual lower peak altitude. On the other hand, in AO2 and AO3, the slit appears to be close or overlap to the main oval at 0.1–0.5 arcsec (2–9 pixels, 330–1500 km) inside from the limb. The flux above the limb may have been be affected by a narrow, brighter region in front of the horizon.

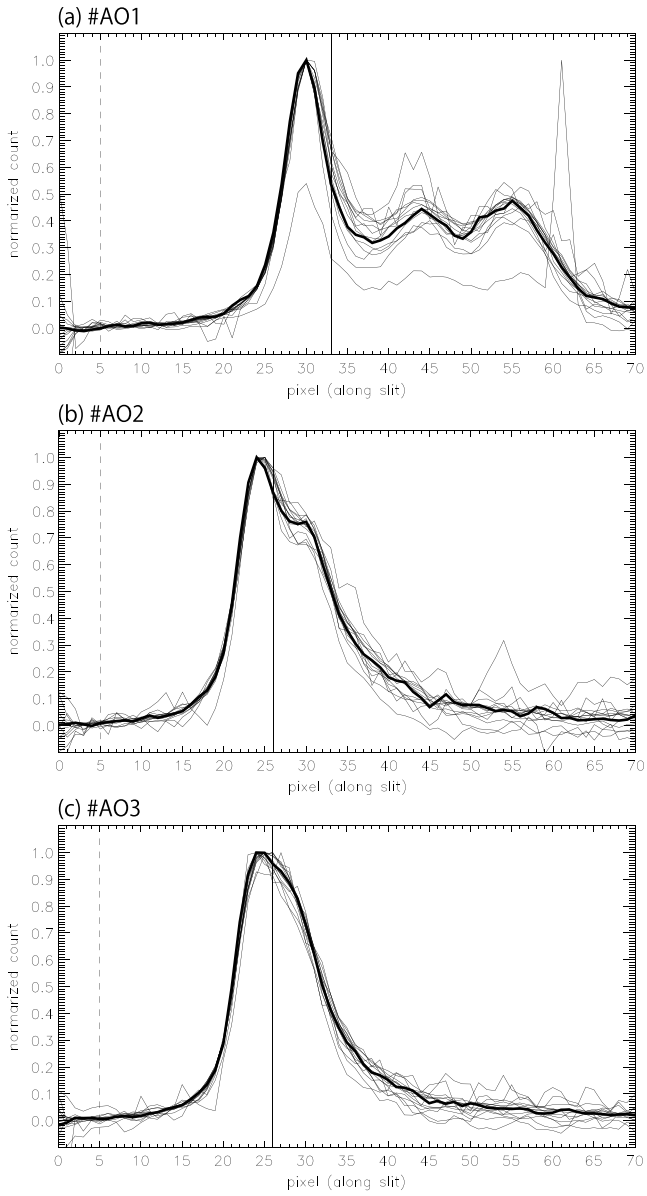

Figure 6. The 15 emission profiles of H_3^+ overtone lines along the slit in the data at (a) AO1, (b) AO2, and (c) AO3. The data shown correspond to the lines marked by asterisk in Table 2. The thick line is the profile of *R*(7,7) line (#34). The *x* axis indicates the pixel number along the slit (1 pixel: 0.055 arcsec, ~165 km at Jupiter). (left) The off-limb direction. The vertical solid lines at $x = 33$ (Figure 6a), 26 (Figure 6b), 26 and (Figure 6c) mark the limb positions. The region to the left of these lines corresponds to above the limb. Vertical dashed lines at the $x = 5$ mark the most distant pixel used for the onion peeling analysis to derive the vertical emission profile. The *y* axis shows the flux normalized by each peak value.

3. Results and Discussions

3.1. Emission Profiles Along the Slit

Figure 6 shows the relative emission profiles along the slit, for 15 H_3^+ overtone emission lines ($v_2 = 2$–0, listed with asterisk in Table 2) for AO1 (Figure 6a), AO2 (Figure 6b), and AO3 (Figure 6c). Figures 7 and 8 show those for 5 H_3^+ hot overtone emission lines ($v_2 = 3$–1, listed with double asterisk in Table 2) and 3 emission lines of H_2 S_1 ($v = 1$–0, listed with triple asterisk in Table 3), respectively. The *x* axis shows the pixel number along the slit (1 pixel: 0.055 arcsec, ~165 km at Jupiter). The left side represents the space observed above the limb, and the right side represents the Jovian disk. The limb-brightening peak positions are shown by the solid lines at $x = 33$ in AO1 and $x = 26$ in AO2 and AO3. The dashed lines at $x = 5$ indicate the outermost pixel used for the onion peeling analysis. The *y* axis shows the intensity profile of each line with ±3 pixel binning along the wavelength direction and is normalized by the peak value.

In the horizontal distributions inside the Jovian disk, H_3^+ and H_2 emissions had different horizontal morphologies which were also seen in previous studies [*Raynaud et al.*, 2004; *Chaufray et al.*, 2011; *Uno*, 2013]. In the H_3^+ overtone profile (Figure 6), AO1 shows that the area between pixel #40 (~0.4 arcsec (~1200 km) from the limb) and pixel #55 (~1.2 arcsec (~3600 km) from the limb) has higher counts contributed by the bright aurora around the expected main oval location (~1.1–1.3 arcsec (3300–4000 km) from the limb as seen in Figure 5a). The area closer to the limb appears to be dominated by weaker emission from the polar cap area (Figure 5a). In AO2, the area from the limb to pixel #32 (~0.3 arcsec (900 km) from the limb) is relatively bright because of the possible contribution from the region close to the expected main oval location (~0.1–0.5 arcsec (330–1500 km) from the limb as seen in Figures 5b and 5c). AO3 also shows less but similar enhancement around pixel #32. For the H_3^+ hot overtone emissions (Figure 7), although the emission profiles are noisier due to the weaker signal, the profiles in the disk are similar to those of the H_3^+ overtone lines in Figure 6. On the other hand, the horizontal profile of H_2 emissions (Figure 8) exhibits different structures inside the disk. In AO1, the bright auroral area (pixels #40–55, ~0.4–1.2 arcsec (~1200–3600 km) from

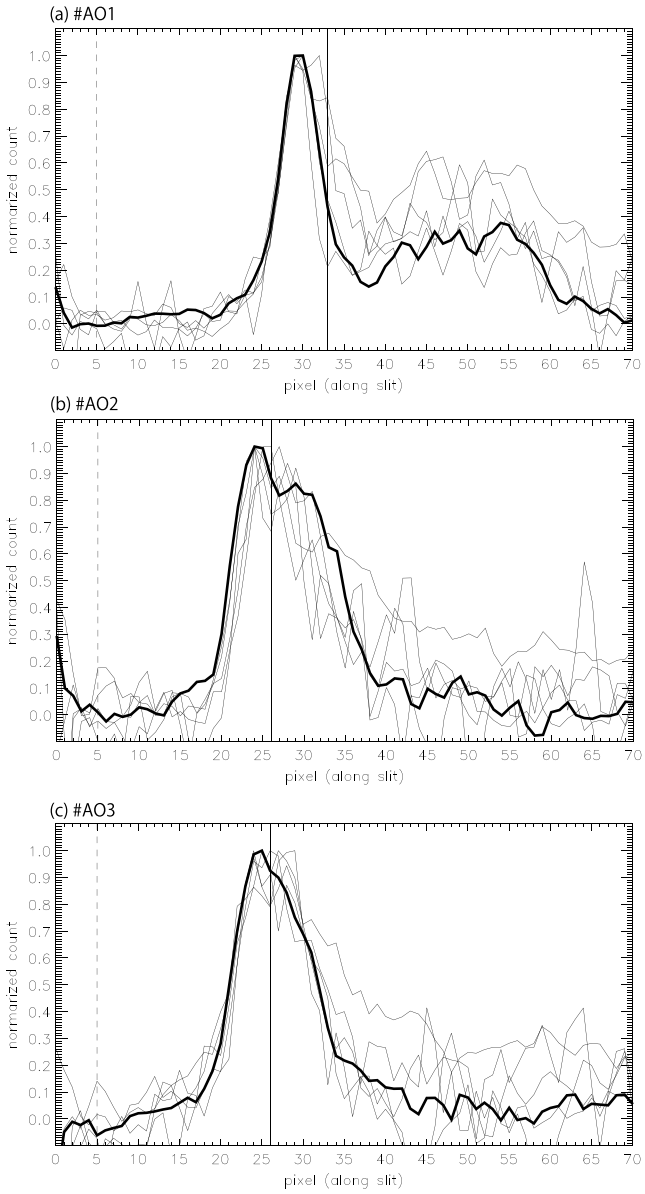

Figure 7. The 5 emission profiles of H_3^+ hot overtone lines along the slit in the data at (a) AO1, (b) AO2, and (c) AO3. The data shown correspond to the lines marked by double asterisk in Table 2. The thick line is the profile of *R*(5,6) line (#31). The plotting format is the same as Figure 6.

the limb) is also enhanced but shows lower contrast without the double-peak feature shown in the H_3^+ overtone lines in Figure 6. In both AO2 and AO3, the area close to the limb (pixel #32) does not show the enhancement appearing in the H_3^+ lines (Figures 6 and 7). The analyses of these differences in the horizontal aurora profile between H_3^+ and H_2 are left for future research.

Vertical emission profiles, the main target of this paper, are contained in the flux distribution above the limb. Smaller morphological differences are present between H_3^+ and H_2 emissions than that predicted by models and estimated from the different temperatures, velocity fields, and morphologies. In Figure 6 (H_3^+ overtone), Figure 7 (H_3^+ overtone), and Figure 8 (H_2), the emission peak positions are similar, i.e., at ~1–3 pixels (~170–500 km) above the limb position for the H_3^+ overtone lines, ~1–4 pixels (~170–660 km) for the H_3^+ hot overtone lines, and ~2–3 pixels (~330–500 km) for the H_2 lines. The scale heights above the flux peak location are also similar, i.e., ~3–3.5 pixels (~500–580 km) for the H_3^+ overtone lines, ~2.5–3.5 pixels (~410–580 km) for the H_3^+ hot overtone lines, and ~2.5–3.5 pixels (~410–580 km) for the H_2 lines. Although the H_3^+ hot overtone profiles contain larger errors, their vertical emission profiles do not differ significantly from the H_3^+ overtone profiles.

As we mentioned, these flux peak positions above the limb can appear at the region closer to the limb than the actual emissivity peak altitude if bright and narrow main oval emission is in front of or behind the limb. This "virtual lower peak altitude effect" might be 0.04–0.19 arcsec (0.7–3.5 pixels, 110–580 km) in AO1, and 0.1–0.5 arcsec (2–9 pixels, 330–1500 km) in AO2 and AO3, estimated by the expected main oval location shown in Figure 5.

In AO2 and AO3, it is likely because the H_3^+ flux in Figure 6 and Figure 7 shows large flux in the region just above the limb, which suggests the bright source in front of the limb as described above. However, this characteristic is not clear in the H_2 flux shown in Figure 8. On the other hand, in AO1, the enhancement of the flux in the region just above the limb is not seen in both H_3^+ and H_2 emissions. It suggests that the main auroral oval behind the limb is very close to the horizon or might not be much brighter than the long integrated flux of polar diffuse aurora. We will investigate this bias effect again in the vertical emissivity profile extracted by the onion peeling method. We also note that the relative difference in the peak altitudes and the scale height between H_3^+ and H_2 emissions should not be affected by this effect.

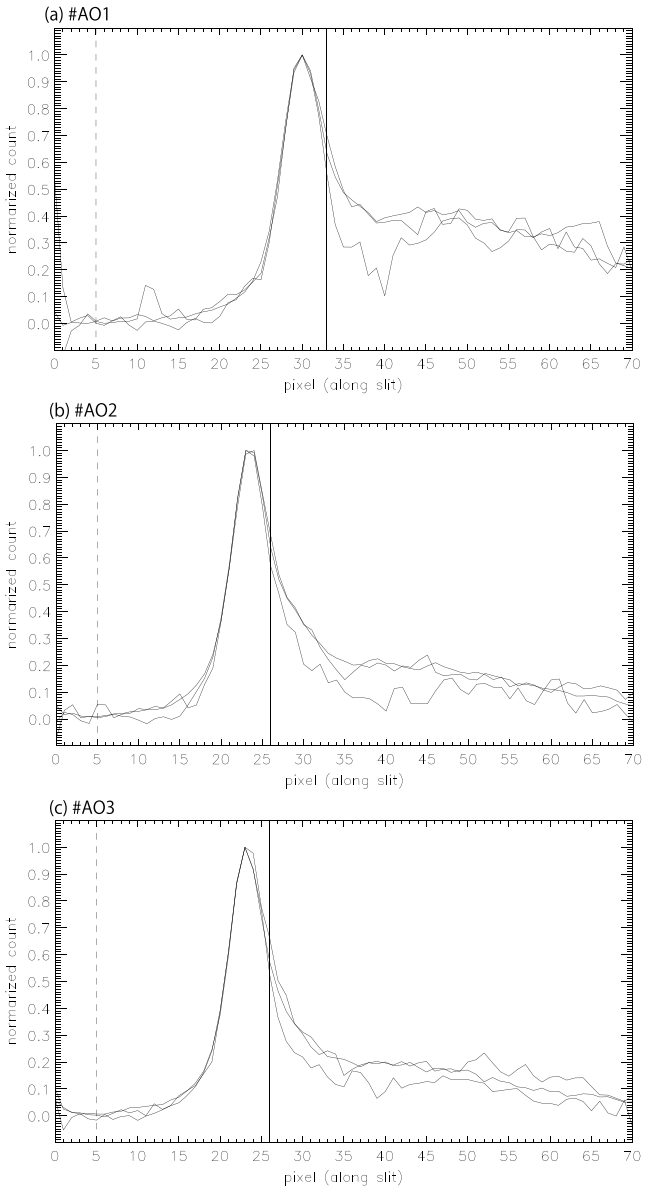

Figure 8. The 3 emission profiles of H_2 S_1 lines along the slit in the data at (a) AO1, (b) AO2, and (c) AO3. The data shown correspond to the lines marked by triple asterisk in Table 3. The plotting format is the same as Figure 6.

3.2. Vertical Profiles Derived by the Onion Peeling Method

Figures 9, 10, and 11 show the vertical volume emissivity profiles extracted by the onion peeling method [*Lystrup et al.*, 2008] with the resolution of 1 pixel size (~165 km). Figure 9 shows those of 15 H_3^+ overtone lines in AO1 (Figure 9a), AO2 (Figure 9b), and AO3 (Figure 9c) extracted from the slit image data in Figure 6. Figure 10 shows those of 5 H_3^+ hot overtone lines extracted from the data in Figure 7. Figure 11 shows the profiles of 3 H_2 lines extracted from the data in Figure 8. In each figure, the *x* axis shows the volume emissivity normalized by the peak value of each profile, and the *y* axis shows the altitude above the limb position in kilometers. The thick gray lines indicate their averaged profiles. In these figures, the peak altitudes are similar for all lines, i.e., ~600 + −100 km for H_3^+ overtone, ~570 + −100 km for H_3^+ hot overtone (with larger error than other lines), and ~650 + −70 km for H_2 in AO1–AO3 cases. In all of these lines, the peak altitudes in AO2 and AO3 are lower than that in AO1, with the difference of 150–250 km for H_3^+ overtone, 200–300 km for H_3^+ hot overtone, and 100 km for H_2.

Before the evaluation, we should consider the virtual lower peak altitude effect as mentioned in sections 2.2 and 3.1, which are caused by bright, narrow main oval emissions in front of or behind the limb position. As described in section 3.1, we estimated by the expected main oval location shown in Figure 5 that this lower peak altitude bias is possible to reach ~110–580 km in AO1 (by the main oval behind the limb) and ~330–1500 km in AO2 and AO3 (by the main oval in front of the limb), depending on the main oval model. In AO1, Figures 9–11 commonly show that the volume emissivity at the altitude below ~400 km from the peak is $<=$ 50% of the peak emissivity. It suggests that the main auroral oval behind the limb does not virtually illuminate this low-altitude area, because it was not much brighter than the long integrated flux of polar diffuse aurora or was very close to the limb. We also expected that if we saw the emission peak created by bright main oval not just above the limb position, we could also see "the secondary enhancement" above, created by long integrated flux of diffuse aurora close to the limb position. Since we do not see this signature in AO1 data, we expect that the lower peak altitude bias can be 0~−330 km (0~2 pixels) scale. On the other hand, in AO2 and AO3, Figure 9 and Figure 10 similarly show that H_3^+ emissivity was larger at altitudes below the peak, which suggests the contribution of the main oval in front of the limb. Their wider peak profile than AO1 might also support it. However, we also

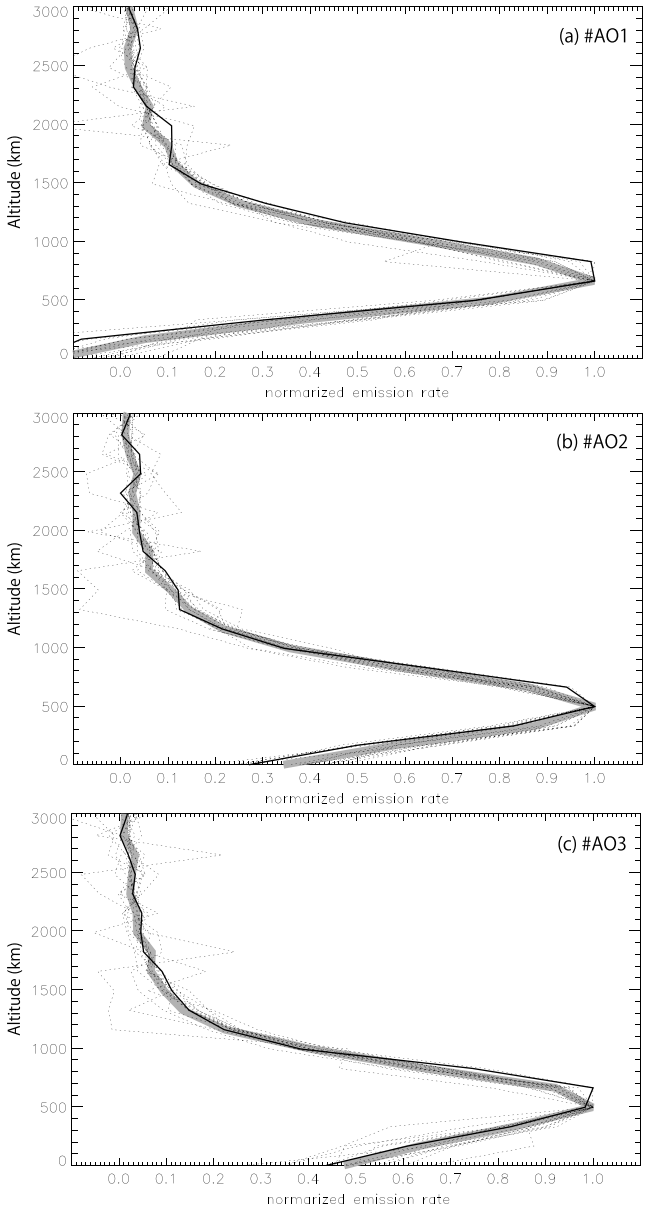

Figure 9. Vertical profile of 15 H_3^+ overtone lines ($v_2 = 2 \rightarrow 0$) derived by the onion peeling method from the observed profiles in Figure 6 at (a) AO1, (b) AO2, and (c) AO3. The *x* axis indicates the volume emissions normalized by the peak value. The *y* axis is the altitude above the limb position (expected at the altitude of ~200(±100) km from 1 bar level) in kilometer. The data shown correspond to the lines marked by asterisk in Table 2. The solid line is the profile of *R*(7,7) line (#34). The thick gray lines are the averages of all profiles.

note that in the emissivity profile of H_2 emission (Figure 11), the volume emissivity at the altitude ~400 km below the peak is $<=$ 50% of the peak emissivity as seen in AO1. If this H_2 emissivity profile is real, it suggests that the peak altitudes of the H_3^+ emissions in AO2 and AO3 are not much below the real one. It means that in AO2 and AO3 data, we also expect that the lower peak altitude bias can be 0~−330 km (0~2 pixels) scale. In the following analysis, we assume that not all vertical volume emissivity profiles of H_3^+ and H_2 lines in AO1–AO3 depart from the real profile more than 0~−330 km. We also note that the discussions about relative difference in the peak altitudes and the scale height between H_3^+ and H_2 emissions should not be affected by this effect.

Table 4 summarizes the peak emission altitudes and emission scale heights determined by using this method. For peak altitudes, we show two values, the observed altitude from the limb position in Figures 9, 10, and 11 (top) and the expected altitude above the 1 bar level (bottom, in *italics*). Since we took the limb position as the peak altitude of the scattered light from stratospheric polar haze at the altitude of 200(±100) km, the latter values are simply +200 km higher than the former. Therefore, in the latter, the peak altitudes are ~700–900 (±100–130) km for H_3^+ overtone, ~680–950 (±130–180) km for H_3^+ hot overtone, and ~590–720 (±50–130) km for H_2, above the 1 bar level. In all lines, the peak altitudes in AO2 and AO3 are lower than that in AO1, with the difference of 150–200 km for H_3^+ overtone, 250–270 km for H_3^+ hot overtone, and 120–130 km for H_2. The scale heights above the peak altitude are similar in AO1–AO3, i.e., ~400–450 km for H_3^+ overtone, ~350–400 km for H_3^+ hot overtone, and ~400 km for H_2.

We compared these H_3^+ vertical profiles to the model profile of *Melin et al.* [2005]. For the overtone and hot overtone H_3^+ emissions, the peak altitude above the 1 bar level and the scale height from the peak derived from our observation are similar to or higher than the model values for the H_3^+ fundamental line, ~500–600 km in the LTE and non-LTE cases. However, these values are lower than the model values of H_3^+ overtone and hot overtone emissions that are emitted in higher-temperature

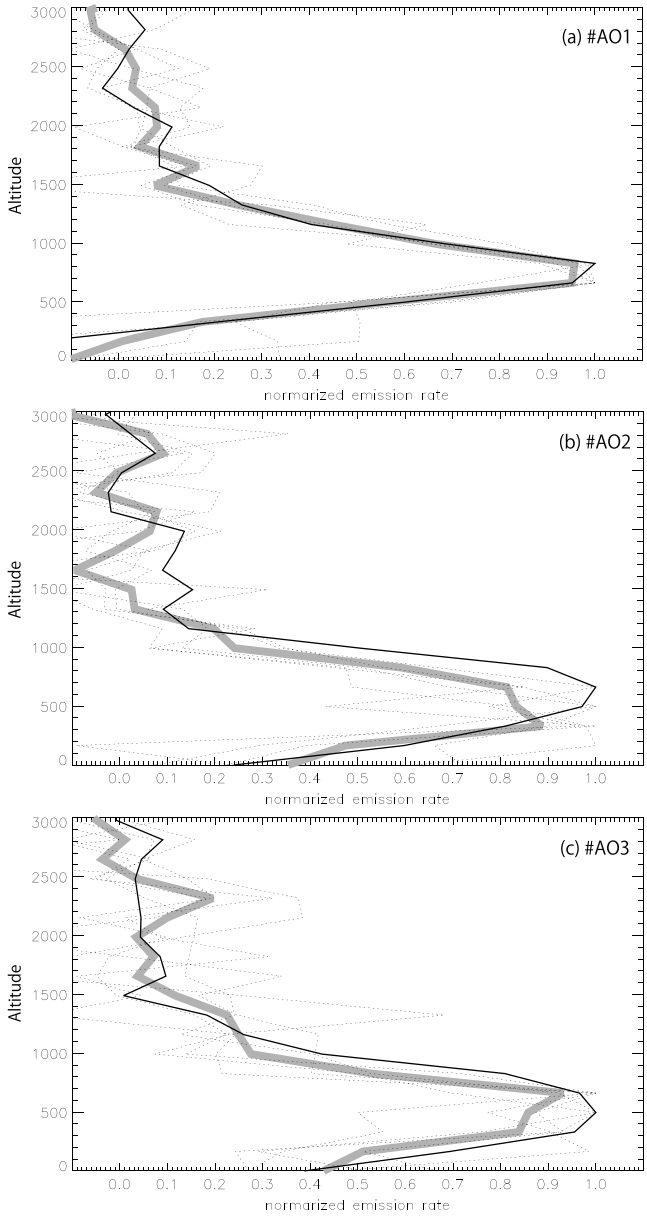

Figure 10. Vertical profile of 5 H_3^+ hot overtone lines ($v_2 = 3 \rightarrow 1$) derived by the onion peeling method from the observed profiles in Figure 7. The data shown correspond to the lines marked by double asterisk in Table 2. The solid line is the profile of *R*(5,6) line (#31). Other parameters are the same as Figure 9.

environments than the fundamental emission. In *Melin et al.* [2005] with the non-LTE effect, the peak altitudes were found to be ~1000 km for H_3^+ overtone and ~1100 km for H_3^+ hot overtone lines, and the scale heights above the peak were ~500 km. The observed peak altitude is lower than those model values with a difference of 100–300 km for the overtone lines and 150–420 km for the hot overtone lines, respectively. And in the observed results, the occurrence of the H_3^+ hot overtone at high altitude than the H_3^+ overtone shown in the model was not clear. The scale height derived from the observation was also slightly smaller than the model value with the differences of 50–100 km in the overtone lines and 150–100 km in the hot overtone lines, respectively. These differences are more evident in AO2 and AO3, close to the main oval, than in AO1, the polar cap region. If we compare these values with the model values obtained under LTE conditions, the differences are larger. Although the assumed altitude of the limb position could potentially be increased up to ~300 km (+100 km higher), this would require that the altitude of the brightest limb position was +200 km higher than that of the haze density peak (~90 km above the 1 bar level).

We already suggested that virtual lower peak altitude effect by the bright main oval not at the limb might provide the underestimation of the peak altitude with the bias of 0~−330 km (0~2 pixels) scale. However, we consider that it is not easy to increase the peak altitude more for H_2. We compare the observed profile of H_2 IR emission to the number density of the vibrationally excited H_2 in the model profile of *Cravens* [1987]. The peak altitude of ~790–920 km above the 1 bar level and the scale height of ~400 km derived from our observation are already higher than the case of 1 keV electron precipitation (peak altitude: ~700 km, scale height: ~400 km). Even if we take the 1 keV case, this electron energy is lower than the assumed values, the sum of three Maxwellian distributions with characteristic energies of 22, 3, and 0.1 keV, in the model of *Grodent et al.* [2001].

We attempted to identify possible reasons why the observed peak altitudes of H_3^+ overtone and H_3^+ hot overtone lines were lower than those derived by *Melin et al.* [2005] accounting for non-LTE effect. The model emission profile was based on the vertical atmospheric model of *Grodent et al.* [2001]. In order

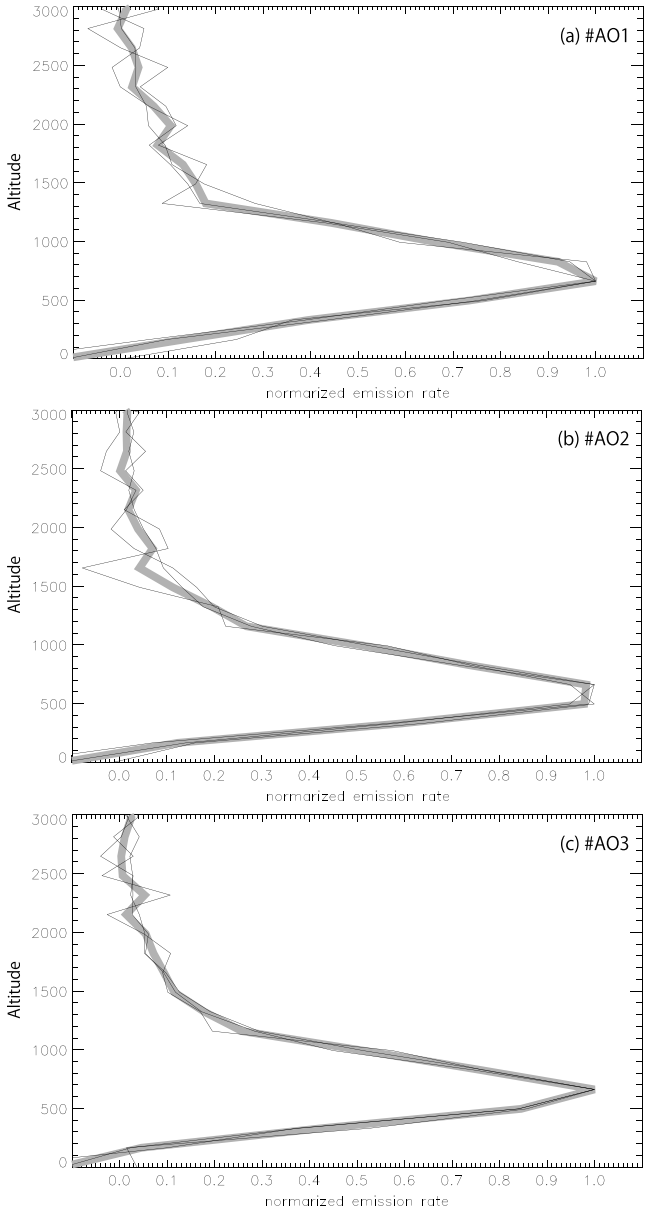

Figure 11. Vertical profile of 3 H_2 lines derived by the onion peeling method from the averaged observed profiles in Figure 8. The data shown correspond to the lines marked by triple asterisk in Table 3. Other parameters are the same as Figure 9.

to decrease the peak emission altitude, the possibilities include (1) higher energy of precipitating electrons that can penetrate into lower atmospheres and enhance more emissions at altitudes below 1000 km, and (2) lower density (lower collision rate) at altitudes below ~1000 km which can reduce the overtone and hot overtone emissions by a stronger non-LTE effect.

For (1), a higher electron energy is contradictory to the observed high H_2 peak emission altitude of ~700–950 km, which suggests that the energy of major precipitated electrons was ~1 keV. It is difficult to explain the lower peak altitude shown in the AO2 and AO3 cases under such lower energy electron precipitation. We note that this effect can contribute to the higher peak altitude of AO1 compared to those of AO2 and AO3. The slit position of AO1 covers the polar cap region in which the precipitating electron energy should be lower than the main oval region close to the slit position of AO2 and AO3. This difference can potentially produce the higher peak altitude of H_2 emission in AO1 from those in AO2 and AO3 with a difference of +100–150 km. The same effect could generate the higher peak altitude of H_3^+ emission in AO1 than those in AO2 and AO3 with a difference of +150–300 km.

To address concept (2), a stronger non-LTE effect compared to that used by *Melin et al.* [2005] requires a lower collision rate at altitudes above ~550 km. This effect can decrease the population in H_3^+ $\nu_2 = 2$ and 3 states at high altitudes, where there are lower collisional excitation rates than the Einstein *A* coefficients, i.e., radiation transition, of H_3^+ overtone (~40–160/s in the analyzed lines marked asterisk in Table 2) and H_3^+ hot overtone transitions (~50–360/s in the analyzed lines marked double asterisk in Table 2). In order to evaluate this effect, we checked the line intensity ratio of the overtone line *R*(7,7) at 2.1131 μm (#34 in Table 2; $A_{if} = 155.4$/s) and the hot overtone line *R*(5,6) at 2.1053 μm (#31 in Table 2; $A_{if} = 346.7$/s) at the altitude of peak flux and volume emissivity. Under a stronger non-LTE effect, a weaker hot overtone line *R*(5,6) could reduce the ratio of *R*(5,6)/*R*(7,7). For example, in the model analysis of *Melin et al.* [2005], the ratio of overtone *R*(6,6) at 2.093 μm to hot overtone *R*(5,6) lines, *R*(5,6)/*R*(6,6), was ~0.33 under non-LTE conditions, smaller than ~0.44 under LTE conditions. The observation of *Raynaud et al.* [2004] showed the flux averaged over the northern auroral region in the nadir line-of-sight integration. In their Figure 1, the ratio of *R*(5,6)/*R*(6,6) was ~0.12 (~5.4×10^{-7} W/m^2/str/cm^{-1} for overtone *R*(6,6) and ~7×10^{-8} W/m^2/str for hot

Table 4. Summary of the Peak Altitude From the Limb Position (Expected at the Altitude of ~200(±100) km From 1 bar Level) and Scale Height Above the Peak Seen in Figures 9–11[a]

	Line	AO1 (Polar)	AO2 (Close to the Edge of Oval)	AO3 (Close to the Edge of Oval)	*Melin et al.* [2005]
Peak altitude	H_3^+ overtone ($\nu_2 = 2 \rightarrow 0$)	~700 + −100 km *(~900 + −100 km)*	~500 + −120 km *(~700 + −120 km)*	~550 + −130 km *(~750 + −130 km)*	*~1000 km (non-LTE)* *~1500 km (LTE)*
	H_3^+ hot overtone ($\nu_2 = 3 \rightarrow 1$)	~750 + −130 km *(~950 + −130 km)*	~500 + −180 km *(~700 + −180 km)*	~480 + −150 km *(~680 + −150 km)*	*~1100 km (non-LTE)* *~1600 km (LTE)*
	H_2	~720 + −100 km *(~920 + −100 km)*	~590 + −130 km *(~790 + 130 km)*	~600 + −50 km *(~800 + −50 km)*	
Scale height	H_3^+ overtone ($\nu_2 = 2 \rightarrow 0$)	~450 km	~400 km	~400 km	*~500 km (non-LTE)* *~600 km (LTE)*
	H_3^+ hot overtone ($\nu_2 = 3 \rightarrow 1$)	~400 km	~350 km	~350 km	*~500 km (non-LTE)* *~600 km (LTE)*
	H_2	~400 km	~400 km	~400 km	

[a]In the peak altitude, lower italic ones show the expected peak altitude from 1 bar level, added simply +200 km to the values in Figures 9–11. The last row are the peak altitude from 1 bar level and scale height of H_3^+ emission models (Figure 6 and Figure 7 in *Melin et al.* [2005]).

overtone *R*(5,6) with d*k* = ~0.2 cm^{-1}), which is lower than the ratio in the non-LTE case of *Melin et al.* [2005]. This result potentially supports the stronger non-LTE effect by a lower collision rate than the model of *Grodent et al.* [2001]. Since *R*(6,6) was in a gap of the echelle order and not included in our observed lines, we used *R*(7,7). We note that in *Raynaud et al.* [2004], the ratio of *R* (5,6)/*R*(7,7) was ~0.21 (~3.4×10^{-6} $W/m^2/str/cm^{-1}$ for overtone *R*(7,7)).

Figure 12 shows the observed flux distribution of lines of the H_3^+ overtone *R*(7,7; thick gray line) and hot overtone *R*(5,6; black line) along the slit in AO1, AO2, and AO3. Figure 13 shows their vertical emissivity profiles derived by the onion peeling method. In both figures, the line strength is not normalized by the peak values. In Figure 12, the flux ratio of *R*(5,6)/*R*(7,7) at the peak flux altitude was ~0.36 in AO1, ~0.20 in AO2, and ~0.21 in AO3, respectively. (At the bright aurora seen in the disk position of AO1 at pixels #40~#55, this ratio is ~0.2.) In Figure 13, the volume emissivity ratio of these lines at the peak emissivity altitude was similar at ~0.37 in AO1, ~0.19 in AO2, and ~0.21 in AO3. The values in AO2 and AO3 are similar to the observed ratio by *Raynaud et al.* [2004] in the flux averaged over the northern auroral region.

3.3. Comparison With the Vertical Profile Model

We compared these observed results with the values reproduced by an emissivity model by *Tao et al.* [2011, 2012]. With the assumed altitude profiles of atmospheric temperature and neutral density, this one-dimensional model estimated the infrared volume flux from H_3^+ produced by auroral electrons (section 2.2 of *Tao et al.* [2011]) and solar EUV (section 2.3 of *Tao et al.* [2011] and section 2.3 of *Tao et al.* [2009]). In order to compare with limb observation of our interest here, we assumed solar zenith angle of 90° for simplicity.

Figure 14 shows the model results. Figure 14a shows three vertical profile models of temperature (solid line), LTE fraction (dash-dotted line, referenced to the temperature *x* axis multiplied by 0.001), and pressure (dashed line), respectively. Figures 14b and 14c show the model emission profiles of H_3^+ overtone *R* (7,7) and hot overtone *R*(5,6) lines under the non-LTE (solid line) and LTE (dotted line) conditions. In all panels, the thick gray lines are based on the atmospheric model condition similar to that of *Grodent et al.* [2001], in which the precipitating electrons are the sum of three Maxwellian distributions with characteristic energies of 22, 3, and 0.1 keV, and the temperature is ~160 K at altitudes below 200 km and ~1320 K above 2000 km. The black lines represents our modified model in which

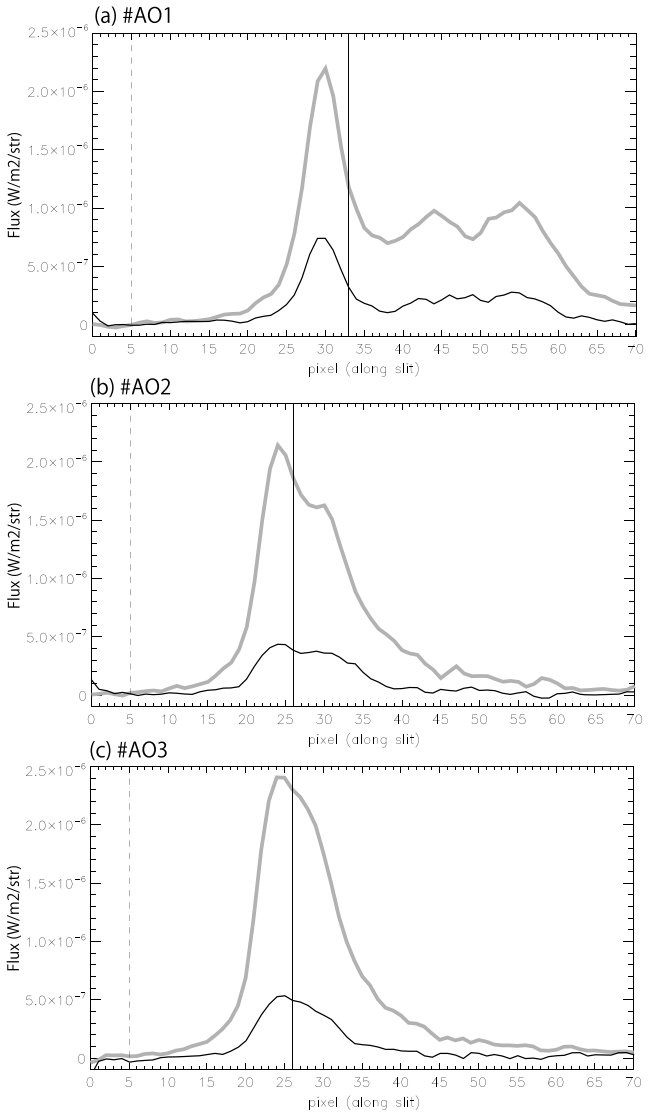

Figure 12. The emission profiles of H_3^+ overtone and hot overtone lines along the slit in the data at (a) AO1, (b) AO2, and (c) AO3. The thick gray line is the profile of overtone *R*(7,7) line (#34). The black line is the profile of hot overtone *R*(5,6) line (#31). The *x* axis is the same as Figure 6. The *y* axis shows the flux in W/m^2/str. The flux ratio *R*(5,6)/*R*(7,7) at the peak is ~0.36 (AO1), ~0.20 (AO2), and ~0.21 (AO3), respectively.

precipitating electrons are modeled as two Maxwellians of 3 keV and 0.1 keV (without the 22 keV components), because our observed peak of H_2 lines suggests an electron precipitation energy of ~1 keV. The red lines represent a further modification from the black lines, in which the temperature was ~160 K at altitudes up to ~350 km and ~1320 K at ~1500 km. Through this modification, we attempted to reproduce the observed lower peak altitudes and the line ratio between overtone and hot overtone lines. In Figures 14b and 14c, we modify the precipitating electron flux to reproduce the peak volume emissivity of *R*(5,6) as ~3×10^{-14} W/m^3/str, close to our observed value shown in Figure 13. This requires a reduction of the precipitating electron flux from the value in *Grodent et al.* [2001] to ~20 nA/m^2 for the gray thick lines (~1/320 of the discrete aurora case in *Grodent et al.* [2001]), ~16 nA/m^2 for the black lines (~1/260), and ~4 nA/m^2 for the red lines (~1/950). We note that the solar EUV flux with the solar zenith angle of 90° has the contribution of ~36% of H_3^+ density at the peak altitude of the vertical H_3^+ emissivity profile. This ratio is reduced to few percent when the solar zenith angle is 95° (behind the limb). We confirmed that in both cases, the vertical emissivity profiles of H_3^+ are similar.

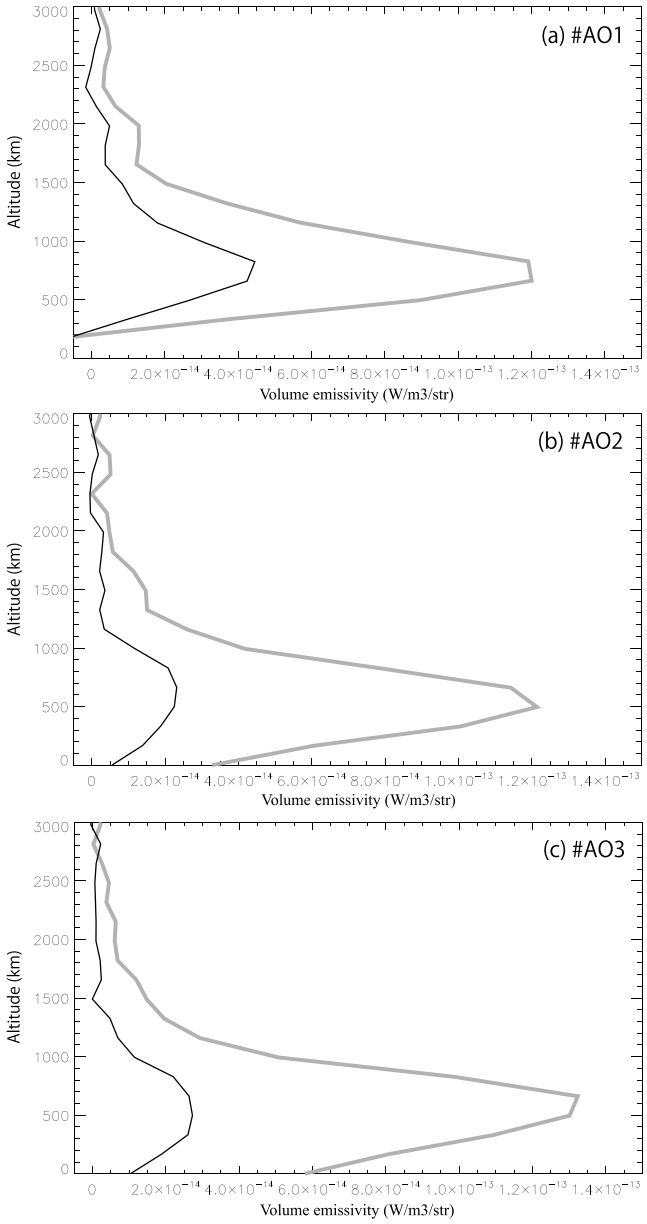

Figure 13. The vertical emissivity profiles of H_3^+ overtone and hot overtone lines derived by the onion peeling method from the observed profiles in Figure 6 at (a) AO1, (b) AO2, and (c) AO3. The thick gray line is the profile of overtone *R* (7,7) line (#34). The black line is the profile of hot overtone *R*(5,6) line (#31). The *y* axis is the same as Figure 8. The *x* axis shows the volume emissivity in W/m^3/str. The emissivity ratio *R*(5,6)/*R*(7,7) at the peak is ~0.37 (AO1), ~0.19 (AO2), and ~0.21 (AO3), respectively.

Considering the gray thick lines representing the conditions of *Grodent et al.* [2001], the peak altitudes of the H_3^+ overtone line *R*(7,7) are ~1400 km (LTE) and ~1050 km (non-LTE), and those of the hot overtone line *R*(5,6) are ~1600 km (LTE) and ~1050 km (non-LTE). These values are not far from the model values in *Melin et al.* [2005] shown for overtone *R*(6,6), rather than *R*(7,7), in their Figure 6 (~1500 in LTE and ~1000 km in non-LTE) and hot overtone *R*(5,6) in their Figure 7 (~1600 in LTE and ~1100 km in non-LTE), within the reading error of the atmospheric conditions and different cross sections of the electron collision process. However, as previously described, these altitudes are higher than our observed values. On the contrary, the emission ratio of *R*(5,6)/*R*(7,7) at the peak altitude becomes ~0.42 (LTE) and ~0.18 (non-LTE). In the non-LTE case, the flux and ratio of these overtone and hot overtone lines correspond to the values derived

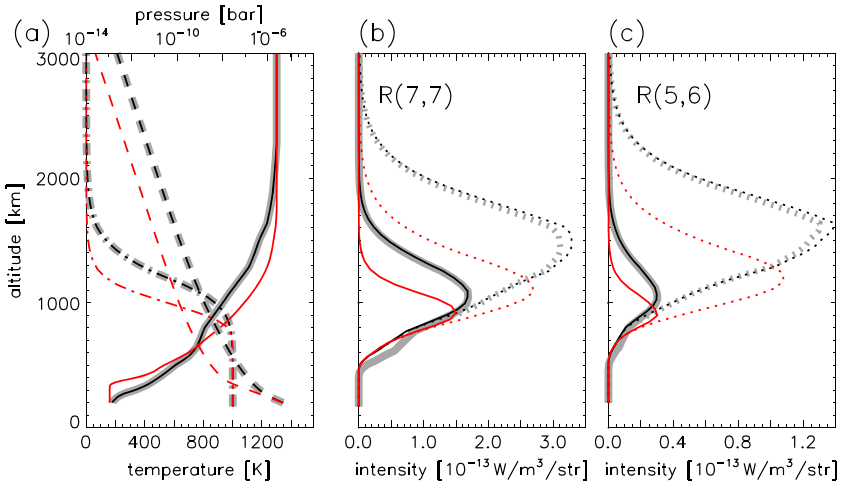

Figure 14. Model altitude profiles of the upper atmosphere and line emissions. (a) Vertical profile model of temperature (solid), LTE fraction (dash-dotted, referenced to the temperature *x* axis multiplied by 0.001), and pressure (dashed), respectively. (b) The model emissivity profiles of H_3^+ overtone *R*(7,7) under non-LTE (solid line) and LTE (dotted) cases. (c) Those of H_3^+ hot overtone *R*(5,6). In all panels, the gray thick lines are the same condition with *Grodent et al.* [2001] in which precipitating electrons consist of the sum of 22, 3, and 0.1 keV and temperature increases from ~160 K at ~200 km to ~1320 K at ~2000 km. The black lines are modified from gray thick lines in which precipitating electrons consist of 3 and 0.1 keV. The red lines are modified from the black lines in which the temperature is ~160 K at ~350 km and ~1320 K at ~1500 km. The electron flux for each case is modified to achieve the observed peak volume emissivity of *R*(5,6), $\sim 3 \times 10^{-14}$ W/m^3/str (see detail in the text).

from our observations in AO2 and AO3 and are smaller than the values in AO1. According to the black lines in which precipitating electrons do not contain the 22 keV components, this modification does not clearly change the peak altitude and the emission ratio of *R*(5,6)/*R*(7,7).

In order to reduce the peak altitudes, for the red lines, we set the temperature at ~160 K at higher altitude up to ~350 km, which reduces the pressure above ~200 km compared to the gray and black lines. This measure enhances the non-LTE effect and reduces the emissivity of flux from the H_3^+ overtone and hot overtone lines in high altitudes. As a result, the peak altitude of H_3^+ overtone and hot overtone lines in the non-LTE case can be less than ~1000 km. Although this modification reduced the emission ratio of *R*(5,6)/*R*(7,7) less than the observed value by a stronger non-LTE effect, we also set the temperature ~1320 K at a lower altitude down to ~1500 km, which enhanced the higher state population of H_3^+ and increased the emission ratio of *R*(5,6)/*R*(7,7). By both temperature modifications, the peak altitudes of the H_3^+ overtone line *R*(7,7) and hot overtone line *R*(5,6) in the non-LTE case became ~950 km and ~900 km, respectively, and their ratio at the peak altitude was ~0.26. These values correspond to our observed values in AO2 and AO3 and are lower than the values in AO1.

This result suggests two factors: (1) In the region outside of the hot main oval such as AO2 and AO3, the temperature at the lower altitude should be less than the values assumed by *Grodent et al.* [2001]. (2) In the polar region such as AO1, the temperature at the lower altitude can be expected to be higher due to adiabatic heating [e.g., *Tao et al.*, 2009]. We will conduct further research to extract the vertical profiles of density, temperature, and line ratio from the observed data and feedback to the polar atmospheric model and the effect on the Jovian MIT coupling system.

3.4. Interpretation of the Similarity in the Vertical Profiles of H_3^+ and H_2

Finally, we discuss the interpretation of the similar source altitudes found for the H_3^+ and IR H_2 emission lines. In our observed results, the H_3^+ overtone (~650–1000 km), H_3^+ hot overtone (~550–1050 km), and IR H_2 emissions (~700–950 km) appeared at similar altitudes. *Chaufray et al.* [2011] showed that the velocity of the H_3^+ ion drift (~3 km/s) was larger than the neutral wind velocity of H_2 (<1 km/s), with the ratio $V(H_2)/V(H_3^+) < 0.33$. They suggested that H_2 emission with lower velocity is from a lower altitude than that of H_3^+ emission with higher velocity. Differences in their auroral morphology also suggest a different source location. However, our result does not show a significant altitude difference.

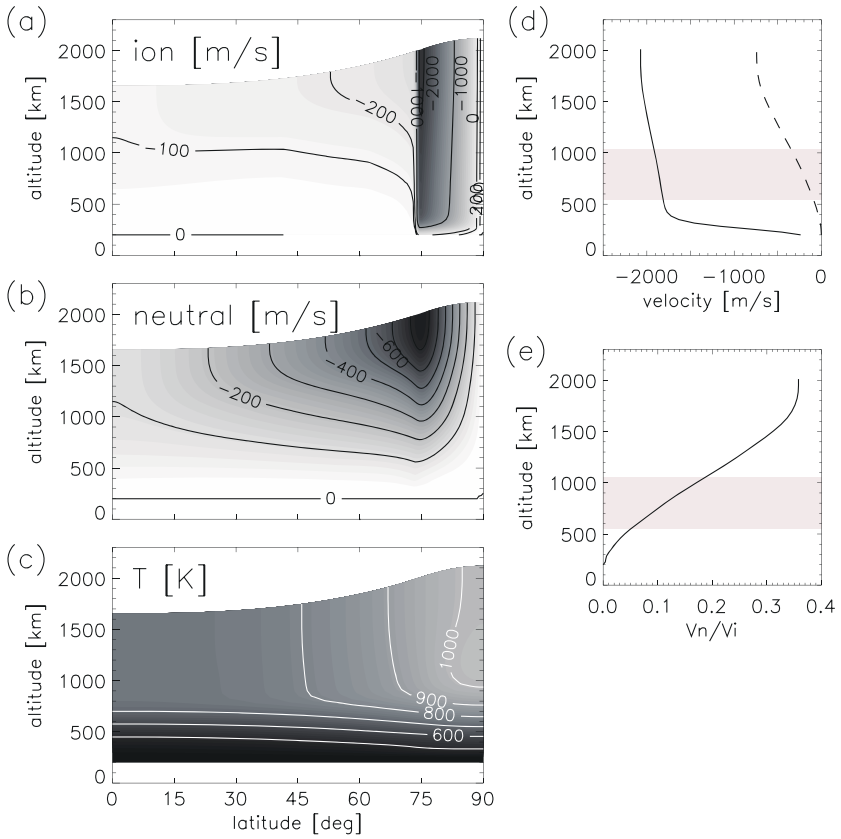

Figure 15. Altitude and latitude distributions of (a) ion zonal wind velocity (m/s), (b) neutral zonal wind velocity (m/s), and (c) temperature (K) and the altitude profiles of (d) ion (thick) and neutral (dashed) wind velocities and (e) their velocity ratio at 75° latitude, estimated using a model by *Tao et al.* [2009]. The ion velocity is estimated from the balance of the dominant terms in the momentum equation for the ion, i.e., the ion-neutral collision and $J \times B$ force terms. In Figures 15d and 15e, the shaded altitude areas (550–1050 km) correspond to the altitude ranges of observed emission peaks of H_3^+ and H_2 K-band lines.

We ran a general circulation model (GCM) of the Jovian upper atmosphere including the physical and chemical processes of the Jovian MIT coupling system, with the effect of the Coriolis force, Joule heating, and auroral processes [cf. *Tao et al.*, 2009]. Figure 15 shows the model output. Figure 15 (left column) shows the altitude and latitude distributions of zonal ion winds (Figure 15a), zonal neutral winds (Figure 15b), and temperature (Figure 15c). Figure 15 (right column) shows the altitude profiles of neutral (dashed line) and ion (solid line) winds (Figure 15d) and their velocity ratio V_n/V_i at the latitude of 75° (Figure 15e). In Figures 15d and 15e, the observed emission altitude range of H_3^+ and H_2, ~550–1050 km, is shaded. The ion velocity was estimated from the balance of the dominant terms in the momentum equation for the ion, i.e., the ion-neutral collision and force terms.

In Figure 15d, the ion and neutral wind velocities at altitudes above ~400 km were ~1800–2000 m/s and several 100 m/s, respectively. Their velocity ratio between the neutral and ion atmosphere, $V(H_2)/V(H_3^+)$, was 0.04–0.37 (Figure 15e). This value is comparable to estimates by other thermosphere models [e.g., *Achilleos et al.*, 2001; *Millward et al.*, 2005] and another MIT coupling model [*Smith and Aylward*, 2009]. We note that the coupling parameter K often referred to in these studies is the ratio of the angular velocity of neutral to magnetospheric plasma Ω_m measured in the frame of the planetary rotation, such that $V(H_2)/V(H_3^+) = \Omega(H_2)/\Omega(H_3^+) \geqq K = \Omega(H_2)/\Omega_m$ for the typical $\Omega(H_3^+) < \Omega_m$ case. The model comparisons are described in *Tao et al.* [2009].

In our observations, the H_3^+ and IR H_2 emissions were from a similar altitude range of ~700 km. This region with high conductivity is the source of the transfer of angular momentum from the planet to the magnetosphere. Our results suggest that using the spectroscopy in the K band, we can potentially determine the coupling

parameter K between neutrals and ions in the Jovian upper atmosphere by measuring the ratio of neutral (H_2) and ion (H_3^+) wind velocities via emissions reported in similar altitudes.

4. Summary

In this paper, we resolved the vertical emission profiles of H_3^+ overtone, H_3^+ hot overtone, and H_2 emission lines in the Jovian northern auroras by using high spatial resolution data obtained by the echelle spectrometer IRCS on the Subaru 8.2 m telescope. The observation was assisted by the AO188, and the spatial resolution achieved was 0.2 arcsec, which is equivalent to ~600 km at Jupiter. The vertical volume emissivity profiles were extracted from the flux distribution of H_3^+ and H_2 emission lines close to the Jovian limb by the onion peeling method.

In the three observed spectra, taken across the polar region (AO1) and at the edge of the main auroral oval (AO2 and AO3), the vertical emission profiles of H_3^+ overtone, H_3^+ hot overtone, and H_2 emissions had similar peak altitudes above the 1 bar level, at ~700–900 (±100–130) km, ~680–950 (±130–180) km, and ~590–720 (±50–130) km, respectively. The observed peak altitudes of H_3^+ overtone and hot overtone lines were lower than the values expected in the model of *Melin et al.* [2005], which are ~1000 km for H_3^+ overtone and ~1100 km for H_3^+ hot overtone lines. Although the lower altitude of H_3^+ might be explained with the lower peak altitude bias with 0~−330 km scale caused by the narrow and bright main oval source in front of or behind the limb position. However, it is hard to explain the high peak altitude of H_2 emissions, which suggest that the precipitating electron energy is low, ~1 keV, which does not penetrate lower altitudes. We concluded that the non-LTE effect in the observed environment could be stronger than expected. We reproduced the observed H_3^+ emissivity profiles from atmospheric model profiles modified after *Grodent et al.* [2001]. The lower peak altitude could have been caused by a stronger non-LTE effect when we set the lower temperature below the altitude of ~350 km. The emission ratio between overtone and hot overtone $R(5,6)/R(7,7)$ lines did not contradict the observation when we enhanced the temperature at an altitude of ~1500 km.

A comparison of our observed results with those of a GCM model suggested that H_3^+ and H_2 could have a large velocity difference at the same altitude region in 550–1050 km. This suggests that the coupling parameter between neutrals and plasma in the Jovian upper atmosphere at an altitude of ~700 km could be observed via K-band spectroscopy by measuring the line-of-sight Doppler shift velocities of H_3^+ and H_2 emission lines.

Including the virtual lower peak altitude effect, the conclusions of this paper have several ambiguities. We will further study these issues including the data taken in 2012–2014.

Acknowledgments

This paper is based on the data collected by using the Subaru telescope, which is operated by the National Astronomical Observatory of Japan (NAOJ). Observed data are opened on Subaru–Mitaka Okayama–Kiso Archive System: http://smoka.nao.ac.jp/) operated by NAOJ. We express our thanks to T.-S. Pyo and Y. Minowa for their kind advice and helpful support for the operation of IRCS and AO188. Y.K. also thanks Hiromasa Nozawa for his kind assistance in creating the main oval position plots. This work is supported by a grant-in-aid for Scientific Research (22340142, 22540255, and 24403007) from the Japan Society for the Promotion of Science and by the Tohoku University Global COE program titled "Global Education and Research Center for Earth and Planetary Dynamics." S.V.B. is supported by a Royal Astronomical Society Research Fellowship.

Alan Rodger thanks the reviewers for their assistance in evaluating this paper.

References

Achilleos, N., S. Miller, R. Prange, G. Millward, and M. K. Dougherty (2001), A dynamical model of Jupiter's auroral electrojet, *New J. Phys.*, 3.1–3.20.

Badman, S. V., G. Branduardi-Raymont, M. Galand, S. L. G. Hess, N. Krupp, L. Lamy, H. Melin, and C. Tao (2014), Auroral processes at the giant planets: Energy deposition, emission mechanisms, morphology and spectra, *Space Sci. Rev.*, doi:10.1007/s11214-014-0042-x.

Chaufray, J.-Y., T. K. Greathouse, G. R. Gladstone, J. H. Waite Jr., J.-P. Maillard, T. Majeed, S. W. Bougher, E. Lellouch, and P. Drossart (2011), Spectro-imaging observations of Jupiter's 2 μm auroral emission. II: Thermospheric winds, *Icarus*, *211*, 1233–1241.

Cohen, I. J., and J. T. Clarke (2011), Modeling of Jupiter's auroral curtain and upper atmospheric thermal structure, *J. Geophys. Res.*, *116*, A08205, doi:10.1029/2010JA016037.

Connerney, J. E. P., M. H. Acuña, N. F. Ness, and T. Satoh (1998), New models of Jupiter's magnetic field constrained by the Io flux tube footprint, *J. Geophys. Res.*, *103*(A6), 11,929–11,940, doi:10.1029/97JA03726.

Cravens, T. E. (1987), Vibrationally excited molecular hydrogen in the upper atmosphere of Jupiter, *J. Geophys. Res.*, *92*, 11,083–11,100, doi:10.1029/JA092iA10p11083.

Dabrowski, I. (1984), The Lyman and Werner bands of H_2, *Can. J. Phys.*, *62*, 1639–1664.

Drossart, P., et al. (1989), Detection of H_3^+ on Jupiter, *Nature*, *340*(17), 539–541.

Grodent, D., J. H. Waite Jr., and J.-C. Gerard (2001), A self-consistent model of the Jovian auroral thermal structure, *J. Geophys. Res.*, *106*, 12,933–12,952, doi:10.1029/2000JA900129.

Hayano, Y., et al. (2008), Current status of the laser guide star adaptive optics system for Subaru Telescope, *Proc. SPIE*, *7015*, id:701510.

Hayano, Y., et al. (2010), Commissioning status of Subaru laser guide star adaptive optics system, *Proc. SPIE*, *7736*, id:77360N.

Kao, L., T. Oka, S. Miller, and J. Tennyson (1991), A table of astronomically important ro-vibrational transitions for the H_3^+ molecular ion, *Astrophys. J. Suppl.*, *77*, 317–329.

Khurana, K. K. (1997), Euler potential models of Jupiter's magnetospheric field, *J. Geophys. Res.*, *102*, 11,295–11,306, doi:10.1029/97JA00563.

Kim, S. J. (1988), Infrared processes in the Jovian auroral zone, *Icarus*, *75*, 399–408.

Kim, S., P. Drossart, J. Caldwell, and J.-P. Maillard (1990), Temperatures of the Jovian auroral zone inferred from 2-micron H_2 quadrupole line observations, *Icarus*, *84*, 54–61.

Kim, Y. H., J. L. Fox, and H. S. Porter (1992), Densities and vibrational distribution of H_3^+ in the Jovian auroral atmosphere, *J. Geophys. Res.*, *97*, 6093–6101, doi:10.1029/92JE00454.

Kobayashi, N., et al. (2000), IRCS: Infrared camera and spectrograph for the Subaru Telescope, *Proc. SPIE*, *4008*, 1056–1066.

Lindsay, C. M., and B. J. McCall (2001), Comprehensive evaluation and compilation of H_3^+ spectroscopy, *J. Mol. Spectros.*, *210*(1), 60–83. [Available at http://h3plus.uiuc.edu/database/.]

Lystrup, M. B., S. Miller, N. Dello Russo, R. J. Vervack Jr., and T. Stallard (2008), First vertical ion density profile in Jupiter's auroral atmosphere: Direct observations using the Keck II telescope, *Astrophys. J.*, *677*, 790–797.

Mallama, A., B. A. Krobusek, D. F. Collins, P. Nelson, and J. Park (2000), The Radius of Jupiter and its polar haze, *Icarus*, *144*, 99–103.

Melin, H., S. Miller, T. Stallard, and D. Grodent (2005), Non-LTE effects on H_3^+ emission in the jovian upper atmosphere, *Icarus*, *178*, 97–103.

Miller, S., R. D. Joseph, and J. Tennyson (1990), Infrared emissions of H_3^+ in the atmosphere of Jupiter in the 2.1 and 4.0 micron region, *Astrophys. J.*, *360*, L55–L58.

Millward, G., S. Miller, T. Stallard, N. Achilleos, and A. D. Aylward (2005), On the dynamics of the jovian ionosphere and thermosphere. IV. Ion-neutral coupling, *Icarus*, *173*, 200–211.

Minowa, Y., et al. (2010), Performance of Subaru adaptive optics AO188, *Proc. SPIE*, *7736*, id:77363N.

Neale, L., S. Miller, and J. Tennyson (1996), Spectroscopic properties of the H_3^+ molecule: A new calculated line list, *Astrophys. J.*, *464*, 516–520. [Available at http://www.tampa.phys.ucl.ac.uk/ftp/astrodata/h3+/.]

Nichols, J. D., J. T. Clarke, J. C. Gerard, D. Grodent, and K. C. Hansen (2009), Variation of different components of Jupiter's auroral emission, *J. Geophys. Res.*, 114, A06210, doi:10.1029/2009JA014051.

Pyo, T.-S. (2003), IRCS echelle spectrograph and data handling. [Available at http://www.naoj.org/Observing/DataReduction/.]

Raynaud, E., E. Lellouch, J.-P. Maillard, G. R. Gladstone, J. H. Waite, B. Bezard, P. Drossart, and T. Fouchet (2004), Spectro-imaging observations of Jupiter's 2 μm auroral emission. I. H_3^+ distribution and temperature, *Icarus*, *171*, 133–152.

Smith, C. G. A., and A. D. Aylward (2009), Coupled rotational dynamics of Jupiter's thermosphere and magnetosphere, *Ann. Geophys.*, *27*, 199–230.

Stallard, T., S. Miller, G. Millward, and R. D. Joseph (2002), On the dynamics of the Jovian ionosphere and thermosphere. II. The measurement of H_3^+ vibrational temperature, column density, and total emission, *Icarus*, *156*, 498–514.

Tao, C., H. Fujiwara, and Y. Kasaba (2009), Neutral wind control of the Jovian magnetosphere-ionosphere current system, *J. Geophys. Res.*, *114*, A08307, doi:10.1029/2008JA013966.

Tao, C., S. V. Badman, and M. Fujimoto (2011), UV and IR auroral emission model for the outer planets: Jupiter and Saturn comparison, *Icarus*, *213*(2), 581–592.

Tao, C., S. V. Badman, T. Uno, and M. Fujimoto (2012), On the feasibility of characterizing Jovian auroral electrons via H_3^+ infrared line-emission analysis, *Icarus*, *221*(1), 236–247.

Turner, J., K. Kirby-Docken, and A. Dalgarno (1977), The quadrupole vibration-rotation transition probabilities of molecular hydrogen, *Astrophys. J. Suppl.*, *35*, 281–292.

Uno, T. (2013), Vertical and horizontal structures of Jovian infrared aurora: Observations and newly development of echelle spectrometer, PhD thesis, Tohoku Univ., pp. 1–136.

Zhang, X., R. A. West, D. Banfield, and Y. L. Yung (2013), Stratospheric aerosols on Jupiter from Cassini observations, *Icarus*, *226*, 159–171.